Computational Study of Thermal Performance of Shape-Dependent CNT/ Titanium Dioxide/Aluminum Oxide-Sodium Alginate Hybrid Nanofluids for Solar Annular Collectors

M. M. Bhatti[1,2,*], T. Abbas[3], O. Anwar Bég[4] and Tasveer A. Bég[5]

[1] Department of Physics, College of Science, Korea University, 145 Anam-ro, Seongbuk-gu, Seoul, Republic of Korea

[2] Material Science Innovation and Modelling (MaSIM) Research Focus Area, North-West University (Mafikeng Campus), Private Bag X2046, Mmabatho, South Africa

[3] Department of Mathematics, Division of Science and Technology, University of Education, Lahore, Pakistan

[4] Multi-Physical Engineering Sciences Group (MPESG), Dept. Mechanical and Aeronautical Engineering, Corrosion/Coatings Lab, 3-08, SEE Building, Salford University, Manchester, UK

[5] Engineering Mechanics Research, Israfil House, Dickenson Rd., Manchester, UK

INFORMATION

Keywords:
Sodium alginate $(C_6H_9NaO_6)_n$
nanofluids
annular solar collectors
carbon nanotubes (CNTs)
(cylinder)
titanium dioxide TiO_2 (spherical)
aluminum oxide Al_2O_3 (platelet)
finite difference method (FDM)
Nusselt number

DOI: 10.23967/j.rimni.2026.10.80311

SCIPEDIA Revista Internacional de Métodos Numéricos para Cálculo y Diseño en Ingeniería

Revista Internacional Métodos numéricos para cálculo y diseño en ingeniería RIMNI

In cooperation with CIMNE

Computational Study of Thermal Performance of Shape-Dependent CNT/Titanium Dioxide/Aluminum Oxide-Sodium Alginate Hybrid Nanofluids for Solar Annular Collectors

M. M. Bhatti[1,2,*], **T. Abbas**[3], **O. Anwar Bég**[4] **and Tasveer A. Bég**[5]

[1]Department of Physics, College of Science, Korea University, 145 Anam-ro, Seongbuk-gu, Seoul, Republic of Korea

[2]Material Science Innovation and Modelling (MaSIM) Research Focus Area, North-West University (Mafikeng Campus), Private Bag X2046, Mmabatho, South Africa

[3]Department of Mathematics, Division of Science and Technology, University of Education, Lahore, Pakistan

[4]Multi-Physical Engineering Sciences Group (MPESG), Dept. Mechanical and Aeronautical Engineering, Corrosion/Coatings Lab, 3-08, SEE Building, Salford University, Manchester, UK

[5]Engineering Mechanics Research, Israfil House, Dickenson Rd., Manchester, UK

ABSTRACT

Solar direct absorber collectors are increasingly deploying more complex working nanofluids to enhance thermal performance. Hybrid nanofluids with non-Newtonian base fluids offer great promise in this regard. Motivated by these developments, the present article examines theoretically and numerically the thermal convection in a ternary hybrid nanofluid comprising an incompressible non-Newtonian sodium alginate base fluid in the annular gap between a pair of infinite concentric cylinders, as a model of a solar annular collector system. Sodium alginate $(C_6H_9NaO_6)_n$ exhibits distinctive thermophysical characteristics, including enhanced versatility and viscoelasticity, rendering it appropriate for solar energy applications when integrated with hybrid nanoparticles. The Reiner-Rivlin third-grade viscoelastic model is therefore deployed to simulate the non-Newtonian characteristics. Three categories of nanoparticles are featured in the hybrid nanofluid: Carbon nanotubes (CNTs), Titanium dioxide (TiO_2), and Aluminum oxide (Al_2O_3). The nanoparticles are categorized by their specific shapes: Carbon nanotubes exhibit a cylindrical form, Titanium dioxide exhibits a spherical configuration, and Aluminum oxide takes on a platelet shape. The presence of hybrid nanofluids influences both the internal transport characteristics and the heat flux towards the curved boundary and the behavior of nanoparticles with varying shapes is also a critical factor. Both linear and quadratic convection, along with viscous dissipation and heat generation/absorption, are also taken into account. The transformed boundary value problem is solved numerically with a finite difference method. Validation of the computational scheme with

OPEN ACCESS

Received: 06/02/2026

Accepted: 20/03/2026

DOI
10.23967/j.rimni.2026.10.80311

Keywords:
Sodium alginate $(C_6H_9NaO_6)_n$ nanofluids
annular solar collectors
carbon nanotubes (CNTs) (cylinder)
titanium dioxide TiO_2 (spherical)
aluminum oxide Al_2O_3 (platelet)
finite difference method (FDM)
Nusselt number

*Correspondence: M. M. Bhatti (mmbhatti@sdust.edu.cn). This is an article distributed under the terms of the Creative Commons BY-NC-SA license

previous studies is included. Graphical results are provided for the impact of all emerging parameters on transport characteristics. Nusselt number is observed to be elevated with higher Grashof number (thermal buoyancy parameter) and heat generation parameter, whereas this trend is reversed with larger volume fractions of nanoparticles (CNTs, TiO_2, Al_2O_3) and greater values of the quadratic convection parameter. The larger volume fraction of CNTs, TiO_2, and Al_2O_3 nanoparticles strongly modifies viscosity and suppresses velocity magnitudes. The skin friction profile shows an increasing trend, which is greatly influenced by the Grash of number, heat generation parameter, and third-grade fluid parameter. In contrast, the quadratic convection parameter and the introduction of nanoparticles (CNTs, TiO_2, Al_2O_3) tend to reduce skin friction magnitudes.

Nomenclature

$\overline{V}$	Velocity vector
p	Pressure
$\frac{\mathrm{d}}{\mathrm{d}t}$	Material time derivative
r, z	Cylindrical coordinates
g	Gravity
β, β_n	Linear and nonlinear thermal expansion
k_{hnf}	Thermal conductivity
C_p	Specific heat
Q	Heat generation/absorption parameter
C	Reference velocity
$\mathcal{K}$	Constant

Greek Letters

μ_{hnf}	Viscosity of the hybrid nanofluid
$\gamma_1, \gamma_2, \overline{\gamma}_1, \overline{\gamma}_2, \overline{\gamma}_3$	Material moduli
θ	Temperature
θ_m	Reference temperature
δ	Third-grade viscoelastic material (rheological) parameter
$\wp$	Prandtl number
ϵ	Eckert number
Ω	Dimensionless heat generation/absorption parameter
Γ	Grashof (thermal buoyancy) number
Γ_1	Quadratic convection parameter
ϕ_1	*CNTs* volume fraction
ϕ_2	TiO_2 volume fraction
ϕ_3	Al_2O_3 volume fraction

1 Introduction

The demand for sustainable and renewable energy has grown considerably in recent years, accelerating the need to investigate creative solutions to improve renewable energy conversion and storage efficiency. Using solar energy is one of the most pragmatic approaches in this regard, with low environmental impact, scalability, and abundant availability on a global scale. Advanced and

painstakingly perfect thermal management systems are absolutely necessary to improve solar thermal system performance. These systems should be made to be able to store and gather heat as well as to minimize heat transfer losses. Consequently, improving the physical and thermal properties of fluids has become a major focus of research in engineering applications [1–4]. Harrabi et al. [5] investigated the enhancement of flat-plate solar water heater performance using simple and hybrid nanofluids under Tunisian climatic conditions. Transient simulations were performed with TiO_2, MgO, and MgO/MWCNT nanofluids to assess system performance in terms of energy production, solar fraction, and CO_2 emission reduction. The results indicated that nanofluids significantly improved collector efficiency compared with pure water. Specifically, dispersing 0.2% and 0.6% TiO_2 nanoparticles in water reduced auxiliary energy consumption by 47.6% and 60.9%, respectively. The collector produced approximately 1294 kWh annually, meeting nearly 65% of household energy demand. Furthermore, the use of MgO–MWCNT hybrid nanofluids increased the solar fraction by about 5.14%, while 0.6% TiO_2 nanoparticles reduced annual CO_2 emissions by up to 0.829 t, highlighting the environmental benefits of nanofluid-based solar collectors.

Enhancing thermal performance through the use of nanofluids is one of the most exciting techniques that has emerged in the last few decades. Through the process of mixing nanoparticles with sizes ranging from 1–100 nm in base fluids, which may be of either Newtonian or non-Newtonian type, a diverse range of nanofluids can be synthesized. In spite of the fact that the nanoparticles include a vast array of metallic and non-metallic particles, the principal base fluids are restricted to water, oil, sodium alginate and ethylene glycol. It is possible that nanofluids have the potential to greatly improve the convective heat transfer, thermal conductivity, and rheological characteristics of base fluids in contrast to the qualities of conventional fluids. There are a variety of solar energy applications that might benefit from the use of nanofluids, such as solar collectors, photovoltaic thermal systems, thermal energy storage systems, and solar desalination systems [6–8].

Hybrid nanofluids are nanofluids that contain more than two types of nanoparticles in a single base fluid. The main purpose of the hybrid nanofluids is to synergistically utilize the harmonizing characteristics of different materials by achieving a mixture of highly thermally conductive nanoparticles with other nanoparticles that are highly stable and highly dispersible. On the contrary, *ternary* hybrid nanofluids contain three different types of nanoparticles. Compared with single or binary nanofluids, ternary hybrid nanofluids have more optimized heat capacity, viscosity control, higher tunability, better stability, and greater thermal conductivity. Many studies of hybrid nanofluids have been communicated in recent years. Manjunatha et al. [9] delineated the methodology for augmenting heat transmission using hybrid nanofluids characterized by natural convection and variable viscosity. The study found that thermal distribution and fluid flow increase with the rise in the particle volume fraction of the nanoparticles. Abdelaziz et al. [10] elucidated the ramifications of mixed convection, including the mobility of nano and hybrid nanofluids inside a horizontal tube, utilizing a finite volume method to derive numerical solutions. Mandal et al. [11] evaluated the flow of magnetized hybrid nanofluid through a W-shaped porous geometrical design, noting that thermal energy increases substantially when the undulation height at the bottom rises. Islam et al. [12] conducted a numerical investigation of magnetized natural convection in hybrid nanofluids using copper and titanium dioxide nanoparticles. Their study indicated that greater Rayleigh number and volume fraction of hybrid nanoparticles enhance heat flux to the boundary, whereas a stronger magnetic field produces the opposite effect. Scott et al. [13] conducted an experimental investigation on the effects of volume concentration of aluminum oxide and multi-walled carbon nanoparticles. It was noted that heat transmission is markedly improved owing to increased volume fraction (concentration of nanoparticles), whereas natural convection is diminished with greater volume fraction. Yusuf et al. [14] conducted

research on the flow of ionic water-based graphene nanofluid across an elastic surface for solar energy coating applications. They further examined slip conditions and heat radiation flux effects and deployed a finite element approach. Mebarek-Oudina et al. [15] examined the magnetic hybrid nanofluid flow and entropy production inside a porous medium. Their observations indicated that the flow and thermal distributions were enhanced with increasing permeability of the porous medium (Darcy number), nanoparticle shape, and porosity parameters. Conversely, strong flow damping was observed with elevated Hartmann (magnetic) numbers. Baithalu et al. [16] conducted a study examining the magnetic dissipation associated with free convection in the flow of hybrid nanofluids through a circular disc-rotating cone configuration. The bvp4c approach was employed to derive numerical solutions. They showed that the volume fraction of both copper and alumina nanoparticles improves the heat transfer. Sai et al. [17] evaluated the performance of Maxwell hybrid nanofluids along an exponentially stretching elastic cylinder with thermal radiation heat transfer via a machine learning methodology.

Previous research on single nanofluids has confirmed improvements in thermal conductivity. Based on this, hybrid binary nanofluids containing two nanoparticles have further demonstrated synergistic heat transfer improvement. Recently, the focus has switched to ternary hybrid nanofluids, which have even more promise owing to a greater variety of nanoparticle properties which can be strategically combined to boost interactions and fine-tune thermal characteristics. Xuan et al. [18] investigated the thermo-economic performance of TiO_2-Al_2O_3-Cu/water ternary hybrid nanofluids by evaluating shear stress, viscosity, and thermal conductivity at 20°C–60°C in a 0.005–1 vol% range. A sensitivity study for viscosity and thermal conductivity at 1% (vol) revealed that the best mixture ratio is 40:40:20 (TiO_2:Al_2O_3:Cu). This ratio produced the maximum heat conductivity and the lowest viscosity. Due to the differences in nanoparticle sizes and arrangements, hybrid nanofluids outperformed single and binary nanofluids. Mahboobtosi et al. [19] explored the behaviour of ternary hybrid nanofluid inside an elastic cylinder and showed that curvature effects, shape factors, and volume percentage of nanoparticles augment the heat and velocity profiles. Kim et al. [20] studied the magnetohydrodynamic natural convective fluid flow and heat transfer of a ternary-hybrid nanofluid in a partly heated porous cavity, concentrating on the impacts of heat absorption/generation and thermal radiation. Using the Marker-and-Cell computational approach, they examined three nanoparticles dispersed in water or kerosene: molybdenum disulfide, single-walled carbon nanotubes, and silver. With nine nanoparticle combinations investigated, they found that lamina-shaped nanoparticles increased thermal transmission rates by 40.8523%, 36.329%, and 38.7025% compared to sphere-shaped ones, and improved average heat transmission rates by 38.0322%, 33.0464%, and 35.5868%, respectively. This study emphasized that optimizing nanoparticle volume fraction and form parameters improved fluid flow and heat transfer efficiency, especially with lamina-shaped nanoparticles in water under heat sources. Shilpa et al. [21] investigated the consequences of discrete heating on magnetohydrodynamic double-diffusive convection and thermal radiation in ternary hybrid nanofluid flow within a vertical cylindrical annulus. They considered Arrhenius activation energy and chemical reactions. Varatharaj et al. [22] evaluated heat transfer optimization using a ternary hybrid nanofluid including silver (Ag), titanium dioxide (TiO_2), and alumina (Al_2O_3) nanoparticles in water (H_2O). They also examined the influence of first-order boundary slip, thermal radiation, porous media drag, viscous dissipation, and Joule heating on thermal and flow behaviour. They found that boosting radiation and magnetic parameters thickens the thermal boundary layer, and that the hybrid nanofluid's velocity can be controlled by adjusting the magnetic field and nanoparticle volume percentage. Haq et al. [23] studied ternary nanoparticles made of aluminum oxide (Al_2O_3), silicon dioxide (SiO_2), and copper (Cu) in a water (H_2O) and ethylene glycol ($C_2H_6O_2$) solution. They used a

momentum equation featuring Darcy and Forchheimer effects, permeability, and magnetic field drag. The thermal field equation was also formulated to consider thermal radiation, intermolecular friction, and Joule heating. Mass concentration effects were also included i.e., binary chemical processes and activation energy. They used the Runge-Kutta Fehlberg (RKF-45) numerical technique and observed that the velocity fields of ternary hybrid nanofluid and hybrid nanofluid decrease with elevation in Forchheimer drag and Hartmann magnetic number. Elnaqeeb et al. [24] investigated the transport behavior of water-based ternary hybrid nanofluids containing nanoparticles of different shapes and densities in a rectangular closed domain under suction and dual stretching. The governing dimensional equations were transformed into dimensionless form using similarity variables and solved numerically via the shooting method, the fourth-order Runge–Kutta scheme, and MATLAB bvp4c. Their results showed that increasing suction and stretching ratio enhanced the vertical velocity component and the Nusselt number, while reducing the velocity components, temperature, and local skin-friction coefficients. They also found that water conveying CuO, Cu, and Ag nanoparticles produced higher Nusselt numbers than the lighter-particle case because of the larger nanoparticle densities.

In the present analysis, we have considered three different types of nanoparticles, i.e., carbon nanotubes (CNTs) [25], titanium dioxide (TiO_2) [26], and aluminum oxide nanoparticles (Al_2O_3) [27] for hybrid nanofluids. The CNTs are considered cylindrical-shaped, TiO_2 nanoparticles are considered spherical-shaped, while Al_2O_3 nanoparticles are considered platelet-shaped. We have selected this combination of nanoparticles as the cylindrical shape of CNTs shows extraordinary mechanical stability with higher thermal conductivity; spherical shape TiO_2 nanoparticles, although they have moderate conductivity, also possess excellent chemical stability; and platelet-shaped Al_2O_3 nanoparticles can enhance the effective surface area for thermal interaction. Therefore, amalgamating such types of ternary hybrid nanoparticles can tailor the thermal and flow behavior and achieve enhanced performance in potential direct absorber solar energy systems. For the base fluid, we have considered sodium alginate $(C_6H_9NaO_6)_n$ [28] for the present study. Relatively few studies have examined non-Newtonian base fluids such as sodium alginate in concentric cylinders, which is the main focus of the current investigation. Experimental evidence of non-Newtonian characteristics in both nanofluids and hybrid nanofluids has been presented by a variety of researchers [29–36] and these studies have highlighted pseudoplastic, dilatant, viscoplastic and also viscoelastic behaviour at different volume fractions, for a range of nanoparticles (e.g., CNTs, titania, zinc oxides) in different base fluids (polymers, oils, sodium alginate suspensions etc). The justification for including a non-Newtonian model in simulations is therefore clear. Most previous computational studies have considered non-Newtonian effects or the influence of particle morphology. A particularly robust rheological model is the Reiner-Rivlin third-grade viscoelastic model, which has been elaborated in considerable detail by Fosdick and Rajagopal [37]. This model is a *differential-type* viscoelastic model and belongs to the Reiner–Rivlin family of rheological models. It robustly simulates the relationship between the stress history and deformation gradient and accurately models shear thinning (decrease in shear viscosity with increasing shear rate) or shear thickening (elevation in shear viscosity with increasing shear rate) behavior. It also features additional rheological material parameters compared with other popular viscoelastic models, such as the Maxwell, Walters-B, or Oldroyd-B viscoelastic models. via the third-grade model, the relative effects of viscous and elastic forces in nanofluids can be more precisely assessed. This model has been applied in previous studies of rheological unitary (single particle) nanofluids by Hiremath et al. [38] (external nanofluid cylinder coating flow), Reddy et al. [39] (non-Fourier magnetized oscillatory third-grade nanofluid flow in a porous duct), and Hiremath et al. [40] (for supercritical thermophysical nanofluid transport on a curved body with magnetic field). These studies have been confined to the Buongiorno nanoscale formulation and have ignored volume fraction

effects. Also, to the authors' knowledge, the third-grade nanofluid model has not yet been explored for annular ternary hybrid nanofluid internal flows. Therefore, the main objective of the present study is to *examine the hydrodynamic and thermal behavior of ternary hybrid nanofluid flow through the annular gap between infinite concentric cylinders*. While hybrid nanofluids have been widely studied, reports on ternary hybrids remain scarce. Moreover, the role of nanoparticle morphology under quadratic convection and viscous dissipation in a non-Newtonian base fluid has not been addressed significantly in technical studies to date.

This article aims to fill these gaps and to generalize previous investigations to consider sodium alginate $(C_6H_9NaO_6)_n$-carbon nanotubes (CNTs)/titanium dioxide (TiO_2)/aluminum oxide (Al_2O_3) third-grade ternary nanofluid. Shape factor effects are included for different hybrid nanoparticles. The importance of shape factor on transport phenomena in nanofluids has been addressed earlier by, for example, Li and You [41], Ananth Subray et al. [42], Akbar et al. [43], and Hiremath et al. [44]. Again, these studies were restricted to unitary or binary hybrid nanofluids and did not consider ternary nanofluids. This geometry is of considerable interest in the design of solar receivers and heat exchangers. This study has the potential to highlight the balance between fluid mechanical behavior and enhanced heat transfer that are useful for the optimized nanofluid-based solar collectors. Additionally, we have considered quadratic and linear convection with internal heat generation/absorption to provide more refined multi-physics in the mathematical model. The novelties of the present work are the *simultaneous consideration of ternary hybrid nanoparticles* i.e., *carbon nanotubes (CNTs), titanium dioxide (TiO_2), and aluminum oxide (Al_2O_3), sodium alginate ($C_6H_9NaO_6)_n$, base fluid, shape factor effects, a third-grade viscoelastic model for the rheology of the base fluid, thermal buoyancy, viscous heating, heat source/sink, quadratic convection and an annular solar collector geometry*. These have not been addressed collectively in any previous study and constitute an important addition to the scientific literature on computational solar collector nanofluid dynamics. The transformed dimensionless nonlinear boundary value problem is solved with an efficient finite difference method (FDM). Validation with previous studies is included [45]. We present extensive graphical results for all emerging parameters, including velocity distribution, temperature distribution, Nusselt number, and skin friction profiles. The results obtained from the present modeling are useful for optimizing solar thermal systems. It is envisaged that they will provide guidelines for the design and manufacturing of storage units, cooling systems, and high-performance solar collectors utilizing ternary hybrid nanofluids for enhanced thermal performance under demanding conditions.

2 Physical Model and Mathematical Formulation for Annular Viscoelastic Hybrid Nanofluid Flow

We consider the nonlinear convection of a third-grade fluid with thermodynamic compatibility, in the annular gap between two stationary, infinite concentric cylinders (see Fig. 1). Here sodium alginate serves as a base fluid. The Reiner-Rivlin third-grade viscoelastic fluid framework is utilized as the rheological model describing the non-Newtonian characteristics of sodium alginate base fluid. The appropriate constitutive equation for the third-grade fluid stress tensor is stated as follows [37]:

$$\xi = -pI + \mu_{\text{hnf}}\mathcal{A}_1 + \gamma_1\mathcal{A}_2 + \gamma_2\mathcal{A}_1^2 + \overline{\gamma}_1\mathcal{A}_3 + \overline{\gamma}_2(\mathcal{A}_1\mathcal{A}_2 + \mathcal{A}_2\mathcal{A}_1) + \overline{\gamma}_3(\text{tr}\mathcal{A}_1^2)\mathcal{A}_1 \tag{1}$$

here μ_{hnf} represents the viscosity of the hybrid nanofluid, $\gamma_1, \gamma_2, \overline{\gamma}_1, \overline{\gamma}_2, \overline{\gamma}_3$ represents the material modulli, $-pI$ represents the spherical pressure due to incompressibility constraints, and the expressions for kinematic tensors are:

$$\mathcal{A}_1 = \nabla\overline{V} + (\nabla\overline{V})^T, \mathcal{A}_n = \frac{\mathrm{d}}{\mathrm{d}t}\mathcal{A}_{n-1} + \mathcal{A}_{n-1}(\nabla\overline{V}) + (\nabla\overline{V})^T\mathcal{A}_{n-1}, n = 2, 3, \ldots \tag{2}$$

here $\overline{V}$ represents the velocity vector, $\frac{\mathrm{d}}{\mathrm{d}t}$ represents the material time derivative. Eq. (1) is useful for computing shear thinning impact and normal stress. According to Fosdick and Rajagopal [37], when thermodynamic limitations are fulfilled, the fluid becomes asymptotically stable. This means that the kinetic energy corresponding to any arbitrary disturbance diminishes with time. If the fluid movements are thermodynamically compatible, then these motions fulfill the Clausius-Duhem inequality, and if it is envisaged that particular Helmholtz free energy is lowest when the fluid locally at rest ([37]).

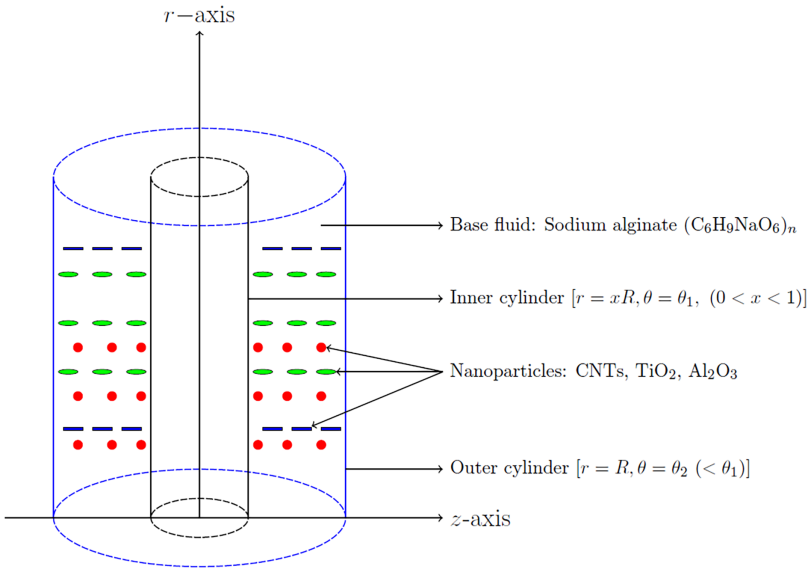

Figure 1: Geometrical structure of hybrid nanofluid flow under the presence of nanoparticles through concentric cylinders

We have:

$$\mu_{\mathrm{hnf}} \geqq 0, \gamma_1 \geqq 0, |\gamma_1 + \gamma_2| \leqq \sqrt{24\mu_{\mathrm{hnf}}\overline{\gamma}_3}, \overline{\gamma}_1 = \overline{\gamma}_2 = 0, \overline{\gamma}_3 \geqq 0 \tag{3}$$

In view of above conditions and assuming that the Eq. (1) is thermodynamically compatible fluid takes the following form as:

$$\xi = -pI + \mu_{\mathrm{hnf}}\mathcal{A}_1 + \gamma_1\mathcal{A}_1 + \gamma_2\mathcal{A}_2 + \overline{\gamma}_3(\mathrm{tr}\mathcal{A}_1^2)\mathcal{A}_1 \tag{4}$$

If the parameters representing normal stress γ_1 and γ_2 are zero, then Eq. (1) takes the following form as:

$$\xi = -pI + \mu_{\mathrm{hnf}}\mathcal{A}_1 + \overline{\gamma}_3(\mathrm{tr}\mathcal{A}_1^2)\mathcal{A}_1 \tag{5}$$

For the current flow configuration, we assume the non-Newtonian fluid described by Eq. (1) represents a sodium alginate-based fluid located in the annular gap between the two concentric vertical cylinders with multiple types of nanoparticles. The nanoparticles comprise carbon nanotubes (CNTs, shape: cylinder), titanium dioxide (TiO_2, shape: spherical), and aluminum oxide (Al_2O_3, shape: platelet). The walls of the outer cylinder are denoted by $r = R$, whereas the inner cylinder is denoted by $r = xR$, where $0 < x < 1$ as shown in Fig. 1. The temperatures at both cylinder walls are constant, but different, and are denoted respectively by θ_2 and θ_1, where $\theta_1 > \theta_2$. Due to the temperature gradient, the

fluid closest to the inner cylinder at $r = xR$ exhibits a higher temperature and then descends under the influence of gravity. In view of the cylindrical coordinate system, we define the velocity and thermal profile in the following form:

$$\overline{V} = \bar{v}(r)e_z, \theta = \theta(r) \tag{6}$$

The mathematical model for nanoparticle effects is developed by extending the earlier study reported by Massoudi and Christie [45] (which neglects nanoparticles, heat generation, quadratic convection etc), and appropriate properties are deployed for platelet aluminum oxide, spherical titanium dioxide, and cylindrical carbon nanotubes in sodium alginate non-Newtonian base fluid. These thermophysical characteristics of nanoparticles and fluid are shown in Table 1. The formulations for determining the properties are given in due course using the Tiwari-Das volume fraction approach which is established as a robust mathematical framework and widely deployed in computational nanofluid dynamics [22,23]. In all cases the hybrid nanofluid is assumed to be a dilute colloidal suspension and agglomeration effects are neglected at any volume fraction. Since the velocity is assumed as $\overline{V} = \bar{v}(r)\mathbf{e}_z$, the flow is fully developed, with $\bar{v}_r = \bar{v}_\theta = 0$ and $\partial/\partial z = 0$; therefore, the convective terms in the momentum and energy equations vanish identically.

Table 1: Thermophysical properties of base fluid and nanoparticles [25,26,28,31]

Base fluid and nanoparticles	ρ (kg m^{-3})	C_p (J kg^{-1} K^{-1})	k (W m^{-1} K^{-1})	$\beta \times 10^{-5}$ (K^{-1})
Sodium alginate $(C_6H_9NaO_6)_n$	989	4175	0.6376	23
Carbon nanotubes (CNTs)	2100	410	3007.4	2
Titanium dioxide (TiO_2)	4250	686.2	8.954	0.9
Aluminum oxide (Al_2O_3)	3970	765	40	0.85

The momentum and energy equations in the component forms for the annular solar collector flow configuration, according to the standard Boussinesq approximation, are articulated as follows:

$$(2\gamma_1 + \gamma_2)\frac{1}{r}\frac{d}{dr}\left[r\left(\frac{dv}{dr}\right)^2\right] = \frac{\partial p}{\partial r} \tag{7}$$

$$0 = \frac{\partial p}{\partial \theta} \tag{8}$$

$$\left.\begin{aligned} &\frac{\mu_{\text{hnf}}}{r}\frac{d}{dr}\left[r\frac{dv}{dr}\right] + 2\overline{\gamma}_3\frac{1}{r}\frac{d}{dr}\left[r\left(\frac{dv}{dr}\right)^3\right] \\ &+ g\left[(\rho\beta)_{\text{hnf}}(\theta - \theta_m) + (\rho\beta_n)_{\text{f}}(\theta - \theta_m)^2\right] = \frac{\partial p}{\partial z}, \end{aligned}\right\} \tag{9}$$

here g denotes gravity, β and β_n signify linear and nonlinear thermal expansion, respectively, and θ_m indicates the reference temperature $\left(\text{in our case, we define it as } \theta_m = \frac{\theta_1 + \theta_2}{2}\right)$. The flow is generated from thermal buoyancy effects or temperature differentials, as shown in Eq. (9). Owing to an indeterminate pressure distribution, we need an extra boundary condition. Given that there is no net flow, either downward or upward, between these two lengthy concentric cylinders, we have:

$$\int_0^{2\pi}\int_{xR}^{R} vrdrd\theta = 0 \tag{10}$$

The aforementioned requirement is obligatory in the absence of net flow. The energy equation including the effects of viscous dissipation and heat production/absorption can be presented as:

$$\frac{k_{\text{hnf}}}{r(\rho C_p)_{\text{f}}}\frac{d}{dr}\left[r\frac{d\theta}{dr}\right] + \frac{\mu_{\text{hnf}}}{(\rho C_p)_{\text{f}}}\left(\frac{dv}{dr}\right)^2 + \frac{2\overline{\gamma}_3}{(\rho C_p)_{\text{f}}}\left(\frac{dv}{dr}\right)^4 + \frac{Q}{(\rho C_p)_{\text{f}}}(\theta-\theta_m) = 0 \tag{11}$$

here k_{hnf} denotes the thermal conductivity [W/m·K], C_p[Jkg^{-1} K^{-1}] denotes the specific heat, and Q[Wm^{-3}K^{-1}] denotes the heat generation (source) or absorption (sink) parameter. Appropriate boundary conditions prescribed for Eqs. (7)–(11) are defined as:

$$v = 0, \theta = \theta_1, \text{ at } r = xR \tag{12}$$

$$v = 0, \theta = \theta_2, \text{ at } r = R \tag{13}$$

The *dynamic viscosity, thermal conductivity, and cumulative volume fraction of nanoparticles for* ternary hybrid nanofluid are defined as [22–24]:

$$\left.\begin{aligned} \mu_{\text{hnf}} &= \frac{\mu_{\text{nf1}}\phi_1 + \mu_{\text{nf2}}\phi_2 + \mu_{\text{nf3}}\phi_3}{\phi_c}, \\ k_{\text{hnf}} &= \frac{k_{\text{nf1}}\phi_1 + k_{\text{nf2}}\phi_2 + k_{\text{nf3}}\phi_3}{\phi_c}, \\ \phi_c &= \phi_1 + \phi_2 + \phi_3. \end{aligned}\right\} \tag{14}$$

The *density* is computed using the relation [22–24]:

$$\rho_{\text{hnf}} = (1-\phi_c)\rho_{\text{bf}} + \phi_1\rho_{\text{np1}} + \phi_2\rho_{\text{np2}} + \phi_3\rho_{\text{np3}}. \tag{15}$$

Volumetric thermal expansion of the ternary hybrid nanofluid is defined as follows [22–24]:

$$\beta_{\text{hnf}} = (1-\phi_c)\beta_{\text{bf}} + \phi_1\beta_{\text{np1}} + \phi_2\beta_{\text{np2}} + \phi_3\beta_{\text{np3}} \tag{16}$$

Specific heat capacity of the ternary hybrid nanofluid is evaluated with the relation [22–24]:

$$(\rho C_p)_{\text{hnf}} = (1-\phi_c)(\rho C_p)_{\text{bf}} + \phi_1(\rho C_p)_{\text{np1}} + \phi_2(\rho C_p)_{\text{np2}} + \phi_3(\rho C_p)_{\text{np3}} \tag{17}$$

The *dynamic viscosities* for cylindrical, spherical, and platelet nanoparticles are defined, respectively by [22–24]:

$$\left.\begin{aligned} \mu_{\text{nf1}} &= \left(1 + 2.5\phi + 6.2\phi^2\right)\mu_{\text{bf}}, \\ \mu_{\text{nf2}} &= \left(1 + 13.5\phi + 904.4\phi^2\right)\mu_{\text{bf}}, \\ \mu_{\text{nf3}} &= \left(1 + 37.5\phi + 613.6\phi^2\right)\mu_{\text{bf}}. \end{aligned}\right\} \tag{18}$$

In the above eqns. $(\,)_{\text{bf}}$ denotes base fluid, and $(\,)_{\text{np1,2,3}}$ represents the respective three nanoparticles. Similarly, the *thermal conductivities* for cylindrical, spherical, and platelet nanoparticles are computed with [22–24]:

$$\left.\begin{aligned} k_{\mathrm{nf1}} &= \left[\frac{-2\phi(k_{\mathrm{bf}}-k_{\mathrm{np1}})+2k_{\mathrm{bf}}+k_{\mathrm{np1}}}{\phi(k_{\mathrm{bf}}-k_{\mathrm{np1}})+2k_{\mathrm{bf}}+k_{\mathrm{np1}}}\right]\times k_{\mathrm{bf}},\\ k_{\mathrm{nf2}} &= \left[\frac{-3.9\phi(k_{\mathrm{bf}}-k_{\mathrm{np2}})+3.9k_{\mathrm{bf}}+k_{\mathrm{np2}}}{\phi(k_{\mathrm{bf}}-k_{\mathrm{np2}})+3.9k_{\mathrm{bf}}+k_{\mathrm{np2}}}\right]\times k_{\mathrm{bf}},\\ k_{\mathrm{nf3}} &= \left[\frac{-4.7\phi(k_{\mathrm{bf}}-k_{\mathrm{np3}})+4.7k_{\mathrm{bf}}+k_{\mathrm{np3}}}{\phi(k_{\mathrm{bf}}-k_{\mathrm{np3}})+4.7k_{\mathrm{bf}}+k_{\mathrm{np3}}}\right]\times k_{\mathrm{bf}}. \end{aligned}\right\} \tag{19}$$

Dimensional Analysis

It is judicious to deploy a dimensional analysis to further develop the suggested mathematical model. The following transformed variables are therefore defined:

$$\tilde{v}=\frac{v}{C},\tilde{r}=\frac{r}{R_0},\tilde{\theta}=\frac{\theta-\theta_m}{\theta_1-\theta_2} \tag{20}$$

where $\tilde{v}$ is dimensionless velocity, $\tilde{r}$ is dimensionless radial coordinate, $\tilde{\theta}$ is non-dimensional temperature function, C denotes the reference velocity. Thus, by virtue of Eq. (20), Eqs. (7) to (13) assume the following forms:

$$\frac{\mu_{\mathrm{hnf}}}{\mu_{\mathrm{bf}}}\left[\frac{d^2\tilde{v}}{d\tilde{r}^2}+\frac{1}{\tilde{r}}\frac{d\tilde{v}}{d\tilde{r}}\right]+3\delta\frac{d^2\tilde{v}}{d\tilde{r}^2}\left(\frac{d\tilde{v}}{d\tilde{r}}\right)^2+\frac{\delta}{\tilde{r}}\left(\frac{d\tilde{v}}{d\tilde{r}}\right)^3+\Gamma\left(\frac{(\rho\beta)_{\mathrm{hnf}}}{(\rho\beta)_{\mathrm{bf}}}\tilde{\theta}+\Gamma_1\tilde{\theta}^2\right)=\mathcal{K} \tag{21}$$

$$\frac{k_{\mathrm{hnf}}}{k_{\mathrm{bf}}}\left[\frac{d^2\tilde{\theta}}{d\tilde{r}^2}+\frac{1}{\tilde{r}}\frac{d\tilde{\theta}}{d\tilde{r}}\right]+\wp\epsilon\frac{\mu_{\mathrm{hnf}}}{\mu_{\mathrm{bf}}}\left(\frac{d\tilde{v}}{d\tilde{r}}\right)^2+\wp\epsilon\delta\left(\frac{d\tilde{v}}{d\tilde{r}}\right)^4+\Omega\wp\tilde{\theta}=0 \tag{22}$$

here $\mathcal{K}$ is a constant which may be determined with the help of Eq. (10). The other dimensionless control parameters featured in the dimensionless momentum (21) and energy (22) eqns., are defined as:

$$\left.\begin{aligned} &\delta=\frac{2\overline{\gamma}_3C^2}{\mu_{\mathrm{bf}}R_0^2},\wp=\frac{\nu_{\mathrm{bf}}(\rho C_p)_{\mathrm{bf}}}{k_{\mathrm{bf}}},\epsilon=\frac{C^2}{(C_p)_{\mathrm{bf}}(\theta_1-\theta_2)},\Omega=\frac{QR_0^2}{\nu_{\mathrm{bf}}(\rho C_p)_{\mathrm{bf}}},\\ &\Gamma=\frac{(\rho\beta)_{\mathrm{bf}}g(\theta_1-\theta_2)R_0^3}{\nu_{\mathrm{bf}}\mu_{\mathrm{bf}}},\Gamma_1=\frac{(\rho\beta_n)_{\mathrm{bf}}}{(\rho\beta)_{\mathrm{bf}}}(\theta_1-\theta_2), \end{aligned}\right\} \tag{23}$$

here δ denotes the third-grade viscoelastic material (rheological) parameter, $\wp$ denotes the Prandtl number, ϵ denotes the Eckert number, Ω denotes the heat generation/absorption parameter, Γ denotes the Grashof (thermal buoyancy) number, and Γ_1 denotes the quadratic convection parameter. The non-dimensional boundary conditions emerge as:

$$\tilde{v}=0,\tilde{\theta}=\frac{1}{2},\ \text{at}\ \tilde{r}=x \tag{24}$$

$$\tilde{v}=0,\tilde{\theta}=-\frac{1}{2},\ \text{at}\ \tilde{r}=1 \tag{25}$$

Furthermore:

$$\int_x^1\tilde{r}\tilde{v}d\tilde{r}=0 \tag{26}$$

3 Numerical Solution and Validation

This section outlines the implementation of a numerical method to solve the coupled nonlinear 2nd order, 4th degree ordinary differential Eqs. (21) and (22), with the pertinent boundary conditions (24)–(26). Initially, one partitions the domain of $\tilde{r}$ into $\mathcal{P}$ intervals, specifically $[\tilde{r}_{i-1}, \tilde{r}_i]$ for $i = 1, 2, 3, \ldots, \mathcal{P}$, each of equal size $h = \dfrac{(1-x)R}{\mathcal{P}}$. The nodes can be expressed as $r_i = xR + ih$. The finite difference formulation for the current model is defined as follows:

$$\mathcal{D}_{\mathcal{O}}\tilde{v}_i = \frac{(1+\mathcal{O})\tilde{v}_{i+1} - 2\mathcal{O}\tilde{v}_i - (1-\mathcal{O})\tilde{v}_{i-1}}{2h} \tag{27}$$

where $\tilde{v}_i = \tilde{v}(r_i)$, and $\mathcal{O} = -1, 0, 1$ denote the *backward, central and forward* finite difference approximations for the first derivative of $\tilde{v}$ at the position r_i, respectively. Proceeding, we discretize Eqs. (21) and (22) in the following manner:

$$\left.\begin{aligned} &\frac{\mu_{\text{hnf}}}{\mu_{\text{bf}}}\left[\mathcal{D}_1\mathcal{D}_{-1}\tilde{v}_i + \frac{1}{\tilde{r}_i}\mathcal{D}_0\tilde{v}_i\right] + 3\delta\mathcal{D}_1\mathcal{D}_{-1}\tilde{v}_i(\mathcal{D}_0\tilde{v}_i)^2 + \frac{\delta}{\tilde{r}_i}(D_0\tilde{v}_i)^3 \\ &+ \Gamma\left(\frac{(\rho\beta)_{\text{hnf}}}{(\rho\beta)_{\text{bf}}}\tilde{\theta}_i + \Gamma_1(\tilde{\theta}_i)^2\right) = \mathcal{K}, \end{aligned}\right\} \tag{28}$$

$$\frac{k_{\text{hnf}}}{k_{\text{bf}}}\left[\mathcal{D}_1\mathcal{D}_{-1}\tilde{\theta}_i + \frac{1}{\tilde{r}_i}\mathcal{D}_0\tilde{\theta}_i\right] + \wp\epsilon\frac{\mu_{\text{hnf}}}{\mu_{\text{bf}}}(\mathcal{D}_0\tilde{v}_i)^2 + \wp\epsilon\delta(\mathcal{D}_0\tilde{v}_i)^4 + \Omega\wp\tilde{\theta}_i = 0 \tag{29}$$

here $i = 1, 2, 3, \ldots, \mathcal{P} - 1$. The algebraic coupled Eqs. (28) and (29), along with their associated boundary conditions (24)–(26), are solved utilizing Newton's method. Considering that the unknown vectors are arranged as $\tilde{v}_1, \tilde{\theta}_1, \tilde{v}_2, \tilde{\theta}_2, \ldots, \tilde{v}_{\mathcal{P}-1}, \tilde{\theta}_{\mathcal{P}-1}$, the Jacobian retains a banded structure, allowing for storage without the need for matrices. The boundary conditions specified in Eq. (26) are addressed using the trapezoidal rule to ensure the precision of the numerical method. The accuracy of the resulting approximation is second-order. By using extrapolation and increasing the number of grid points, we have numerically verified this. Newton's method of convergence requires that the highest norm of the difference between iterations be smaller than a given tolerance. With 10,000 grid points, four iterations were usually required to reach the required accuracy with an absolute tolerance 1.0×10^{-6} and relative tolerance 1.0×10^{-3}. As indicated in Table 2, we have compared our results with those of [45] in order to verify the accuracy of the proposed results. All computations have been executed in MATLAB symbolic software.

Table 2: Numerical comparison of current results with Massoudi and Christie [45] for various values of third-grade fluid parameter δ, Prandtl number $\wp$ and Eckert number ϵ, with $\phi_1 = \phi_2 = \phi_3 = \Gamma_1 = \Omega = 0, x = 0.5$

δ	$\wp \times \epsilon$	$\tilde{v}'(\tilde{r})$ [45]	$\tilde{\theta}'(\tilde{r})$ [45]	$\tilde{v}'(\tilde{r})$	$\tilde{\theta}'(\tilde{r})$
0	0.1	0.05057890	−2.885379	0.0505782933	−2.8853826482
0.5	0.1	0.05052125	−2.885379	0.0505204282	−2.8853826526
1	0.1	0.05045401	−2.885379	0.0504629839	−2.8853826569
2	0.1	0.05035072	−2.885379	0.0503493313	−2.8853826656
0	2	0.05057858	−2.885163	0.0505779714	−2.8851672011
0.5	2	0.05052093	−2.885163	0.0505201075	−2.8851672885

(Continued)

Table 2 (continued)

δ	$\wp \times \epsilon$	$\tilde{v}'(\tilde{r})$ [45]	$\tilde{\theta}'(\tilde{r})$ [45]	$\tilde{v}'(\tilde{r})$	$\tilde{\theta}'(\tilde{r})$
1	2	0.05046369	−2.885164	0.0504626644	−2.8851673756
2	2	0.05035040	−2.885164	0.0503490142	−2.8851675491
0	1	0.05057875	−2.885277	0.0505781408	−2.8852805943
0	2	0.05057858	−2.885163	0.0505779714	−2.8851672011
1	1	0.05046386	−2.885277	0.0504628325	−2.8852806815
1	4	0.05046355	−2.884937	0.0504623281	−2.8849407641

The data set is as follows to achieve a validation with [45]: for various values of the third-grade fluid parameter (δ), Prandtl number ($\wp$), and Eckert number (ϵ), with $\phi_1 = \phi_2 = \phi_3 = \Gamma_1 = \Omega = 0, x = 0.5$ (see Table 2). The current results exhibit exceptional concordance, with similarities observed up to four decimal places. This not only confirms the accuracy of the data but also substantiates the proposed technique.

4 Numerical Results and Discussion

This section addresses the numerical results obtained for velocity, temperature, skin friction, and Nusselt number. Computational software Matlab was employed to generate numerical results for all emerging parameters. Our primary focus is on the impact of the following parameters: *third-grade viscoelastic material fluid parameter* (δ), *Grashof number* (Γ), *quadratic convection parameter* (Γ_1), *CNTs* (ϕ_1), (TiO_2) (ϕ_2), (Al_2O_3) (ϕ_3), *heat generation and absorption parameter* (Ω), *and Prandtl number* ($\wp$). Figs. 2–28 illustrate all the graphical distributions for variation of these parameters. Data is extracted from sources [34,46–48] which corresponds to the assumptions made in this work, namely ternary hybrid solar nanofluids functioning as dilute colloidal suspension and agglomeration effects being neglected at any volume fraction.

4.1 Velocity Profiles

Figs. 2–8 depict the velocity field response to different parameters. Fig. 2 illustrates the influence of the third-grade viscoelastic material parameter (δ) on the velocity distribution. Evidently, a notable decrease in the velocity magnitudes is observed with elevated values of the third-grade fluid parameter, although flow reversal (negative velocity) is never computed. Elevated values of the third-grade fluid parameter indicate shear-thickening effects and demonstrate strain-stress interactions that result in a surge in the hybrid nanofluid's resistance to deformation. Viscous forces dominate over elastic forces. This parameter features in two terms in the reduced momentum Eq. (21), viz, $+3\delta\frac{d^2\tilde{v}}{d\tilde{r}^2}\left(\frac{d\tilde{v}}{d\tilde{r}}\right)^2$ and $+\frac{\delta}{\tilde{r}}\left(\frac{d\tilde{v}}{d\tilde{r}}\right)^3$. A rise in hybrid nanofluid resistance is produced by the elevation in effective viscosity due to larger values of the third-grade parameter; momentum transfer is inhibited between fluid layers with viscoelastic material effects. Strong deceleration is generated in the annular flow and is sustained across the entire gap ($0.2 < r < 1$). Clearly, the flow velocity is a maximum for the Newtonian case, wherein $\delta = 0$ and viscoelastic effects vanish. Viscoelasticity therefore exerts a damping effect on the annular flow of hybrid nanofluid. This trend has also been reported by, for example, Ravikumar et al. [35] and Hiremath et al. [38,39].

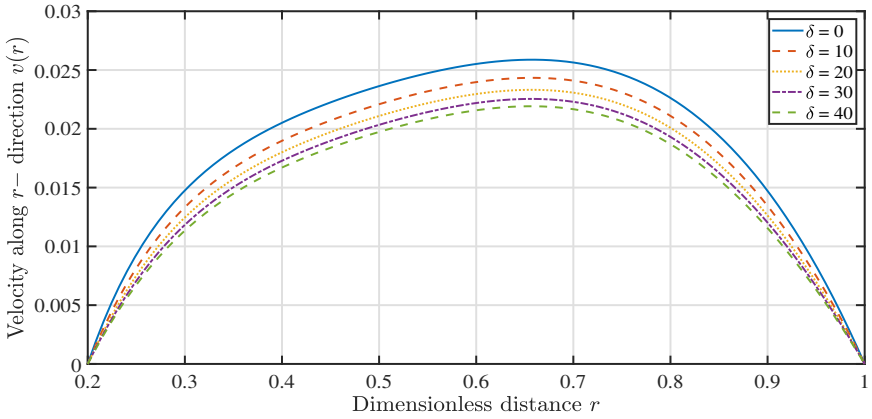

Figure 2: Impact of third-grade fluid (δ) behavior on the velocity profiles

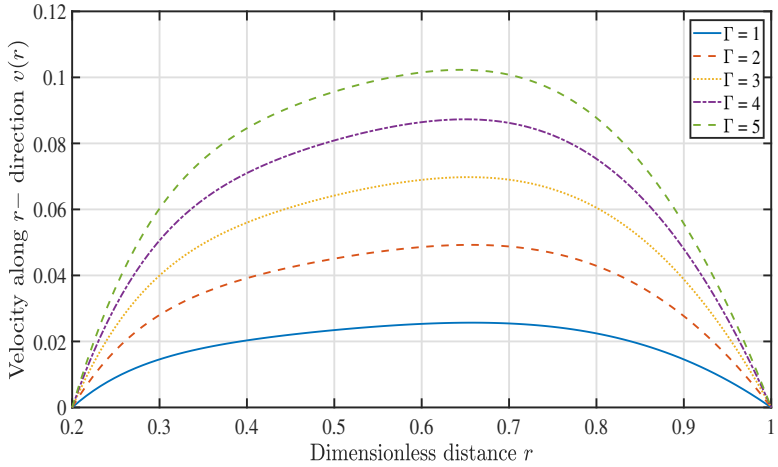

Figure 3: Impact of Grashof number (Γ) behavior on the velocity profiles

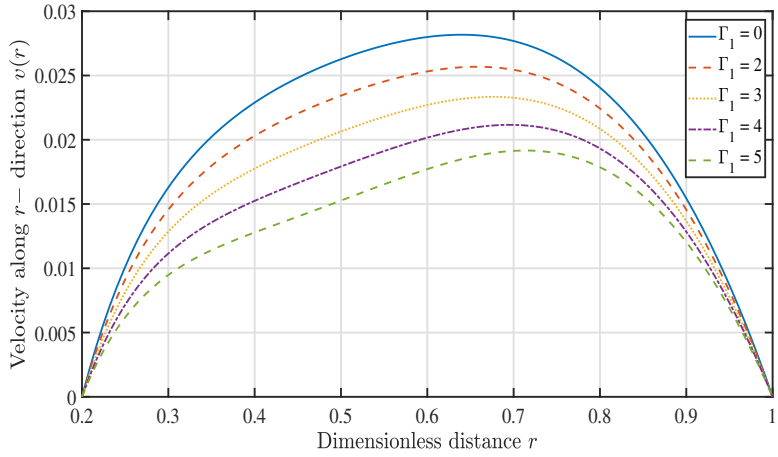

Figure 4: Impact of quadratic convection parameter (Γ_1) behavior on velocity profiles

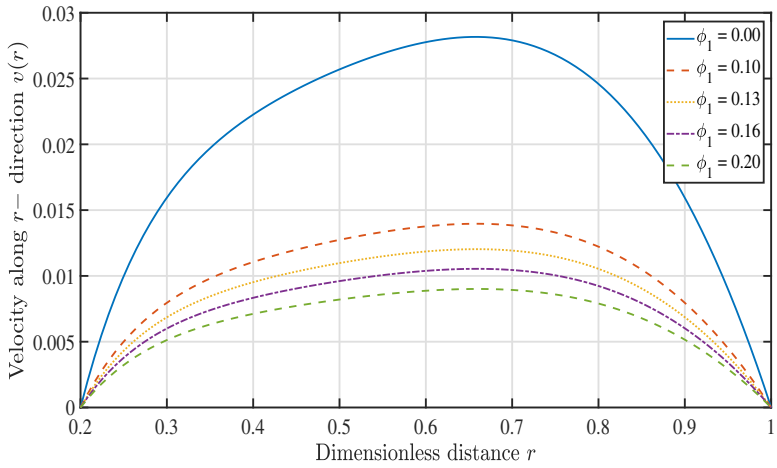

Figure 5: Impact of nanoparticle volume fraction of CNTs (ϕ_1) on velocity profiles

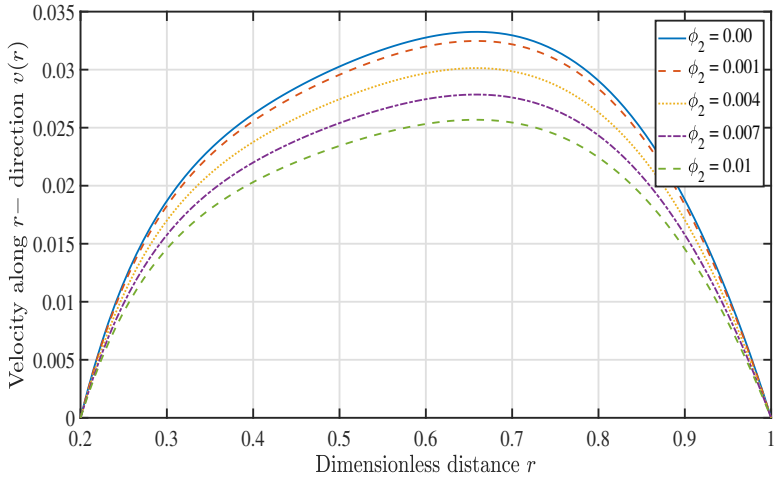

Figure 6: Impact of nanoparticle volume fraction of TiO_2 (ϕ_2) velocity profiles

Fig. 3 demonstrates that elevated Grashof number (Γ) values improve the velocity distribution within the flow of the concentric cylinders. The effects of strong thermal buoyancy are predominant at elevated Grashof numbers ($\Gamma > 1$), leading to an enhancement in fluid motion. Natural convection currents are energized in the annular regime. The buoyancy-driven flow mechanism in solar energy applications offers significant advantages by improving volumetric flux rates in circulation designs via flow acceleration, which assists in achieving optimized thermal performance. Flow deceleration is associated with weak buoyancy ($\Gamma = 1$) for which both viscous and thermal buoyancy forces balance. The influence of thermal buoyancy is therefore a critical factor in solar annular collector designs.

Fig. 4 reveals that velocity magnitudes exhibit a decreasing trend for elevated values of the quadratic convection parameter (Γ_1). Quadratic convection develops in nonlinear buoyancy forces due to a faster progression of temperature differences. High temperature gradients result in quadratic convection, which has a stabilizing influence. Growing values of quadratic convection imply that these stabilization effects suppress flow development, consequently leading to a reduction in the velocity distribution throughout the annular gap. Quadratic convection holds considerable significance in solar

energy applications, particularly in systems operating under vigorous thermal loads, such as solar receivers and solar power collectors, and in extreme environments. The reduction in velocity resulting from the significant influence of quadratic convection signifies that, at elevated temperatures, there might exist a self-limiting mechanism that is valuable in preventing overheating and thermal stress. However, this reducing mechanism in the annulus could restrict the heat transfer process. To achieve optimized thermal performance, it is crucial to manage the quadratic convection parameter while preserving system stability. It is noteworthy that for the special case when the quadratic convection parameter ($\Gamma_1 = 0$), the conventional linear Boussinesq approximation is retrieved, which achieves the maximum velocity. In this case, the generalized quadratic thermal buoyancy term in Eq. (22) reduces from $+\Gamma\left(\frac{(\rho\beta)_{\text{hnf}}}{(\rho\beta)_{\text{bf}}}\tilde{\theta} + \Gamma_1\tilde{\theta}^2\right)$ to the linear Boussinesq model, $+\Gamma\left(\frac{(\rho\beta)_{\text{hnf}}}{(\rho\beta)_{\text{bf}}}\tilde{\theta}\right)$. Effectively, the inclusion of quadratic convection (second-order buoyancy effects) therefore avoids the over-prediction in velocity associated with the standard Boussinesq model.

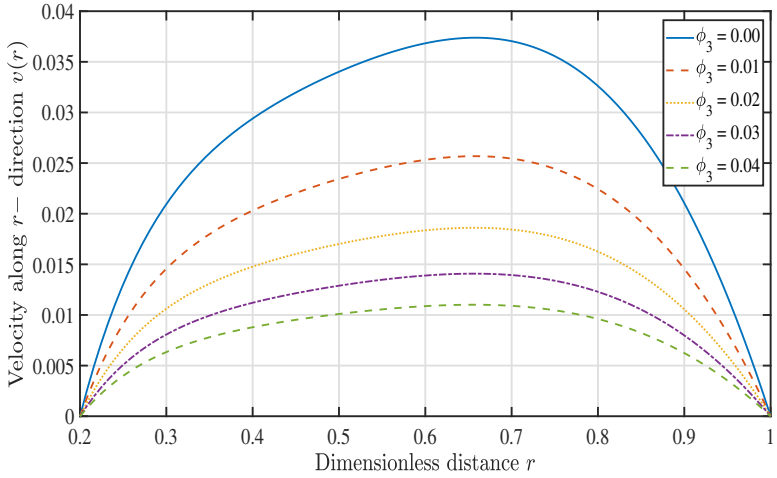

Figure 7: Impact of nanoparticle volume fraction of Al_2O_3 (ϕ_3) velocity profiles

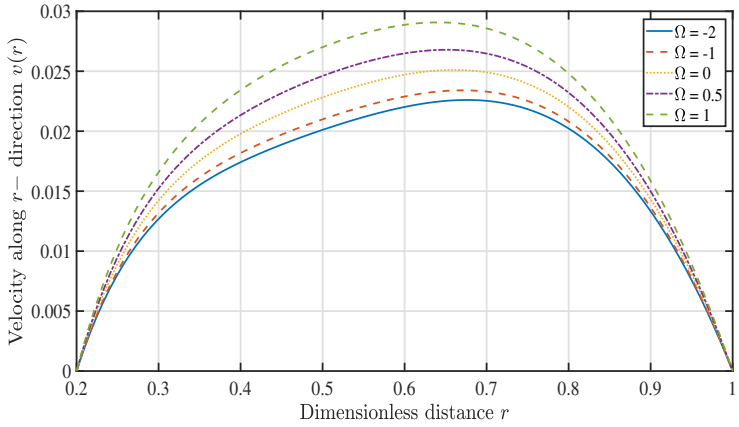

Figure 8: Impact of heat absorption and generation parameter (Ω) velocity profiles

Fig. 5 displays the impact of the volume fraction of cylindrical-shaped carbon nanotubes (CNTs, ϕ_1) on the velocity distribution in the annular regime. It is apparent that the velocity magnitude drops as

the volume fraction of CNTs increases. The presence of cylindrical-shaped carbon nanotubes indicates considerable resistance due to their entanglement mechanism and higher aspect ratio, despite the efforts of the nanotubes to align with the flow. CNTs tend to increase flow resistance, but offer other significant advantages in solar energy applications due to their shape effects and exceptional thermal conductivity, which primarily benefits temperature fields. For the case $\phi_1 = 0$, there are no CNTs present in the hybrid nanofluid, and radial velocity is clearly a maximum across the annular gap.

Fig. 6 depicts the influence of the volume fraction of spherical shaped Titanium dioxide nanoparticles (TiO_2, ϕ_2) on the radial velocity distribution in the annular gap. A greater volume fraction of spherical structured TiO_2 nanoparticles drastically decelerates the annular flow of the third-grade hybrid nanofluid. The spherical structure of TiO_2 nanoparticles demonstrates a moderate shear-thickening (dilatant rheological effect) on the third-grade fluid, and manifests with greater drag across the gap between concentric cylinders. The spherical morphology of TiO_2 nanoparticles contributes positively to the equilibrium between flow performance and thermal conductivity. Furthermore, $\phi_2 = 0$ indicates the absence of a sphere-like shape of TiO_2 nanoparticles, and this produces maximum flow acceleration i.e., greatest velocity magnitudes. It is noteworthy that the disparity between the velocity profiles is less significant than for Fig. 5. (where we plotted volume fraction of cylindrical-shaped carbon nanotubes (CNTs, ϕ_1).

Fig. 7 represents the effects of volume fraction of platelet-shaped aluminum dioxide nanoparticles (Al_2O_3, ϕ_3) on the radial velocity distribution in the annulus. It can be seen that platelet-shaped nanoparticles of Al_2O_3 also suppress the fluid motion across the whole gap between the concentric cylinders. Platelet-shaped nanoparticles Al_2O_3 shows higher rate of hydrodynamic resistance due to their flat geometry and wider surface area, when compared with spherical nanoparticles. This tends to enhance the effective viscosity of the third-grade hybrid nanofluid. Due to their large surface area, platelet-shaped nanoparticles of Al_2O_3 suppress momentum development in the annular gap, which may be beneficial in solar energy applications by prolonging the times achievable for absorption of thermal energy. This shows that their concentration level must be carefully optimized in solar-driven dynamic heat exchangers. Peak velocity is always computed in the absence of platelet-shaped aluminum dioxide nanoparticles (Al_2O_3, $\phi_3 = 0$), indicating that their presence exerts a consistently damping effect on annular flow.

Fig. 8 displays the evolution in radial velocity profiles with a variation in the heat generation/absorption parameter (Ω). It is observed that with increasing positive values of Ω [progressively more intense heat generation], the velocity exhibits a growing pattern across the gap. However, the velocity profile indicates a downward trend for increasingly negative values of Ω [stronger heat absorption]. When the values of $\Omega < 0$, heat absorption (sink) diminishes the available thermal energy that contributes to driving the thermal buoyancy forces. The fluid velocity undergoes a reduction as a result, i.e., annular flow deceleration. Conversely, a positive value of $\Omega > 0$ indicates the occurrence of heat generation, which energizes the regime and assists the buoyancy-driven forces and thermal gradients, leading to a greater magnitude of the velocity profile. This mechanism also holds significant importance in solar energy applications. Molten salt storage tanks and solar thermal collector systems frequently undergo internal heat generation as a result of the chemical reactions induced by concentrated solar input. A higher percentage of internal heat generation enhances convective currents, optimizes overall heat transfer, and improves fluid motion. Consequently, managing the internal heat source in solar-based systems is a vital and efficient technique that can encourage optimal thermal performance.

4.2 Temperature Profiles

The temperature distributions computed against the annular gap are visualized in Figs. 9–16. Fig. 9 illustrates that as the third-grade fluid parameter (δ) is increased, there is a weak depression in temperature magnitudes; the effects are relatively minor, even though there is a direct effect of hybrid nanofluid rheology on the energy Eq. (22), via the fourth degree term, $+\wp\epsilon\delta\left(\frac{d\tilde{v}}{d\tilde{r}}\right)^4$. The primary influence of the third-grade fluid parameter is, as described earlier, on the momentum transfer, i.e., the velocity field, via, for example, the third-degree term, $+\frac{\delta}{\tilde{r}}\left(\frac{d\tilde{v}}{d\tilde{r}}\right)^3$ in the momentum Eq. (21). For a given Prandtl number, the modification in momentum diffusivity will also induce changes in thermal diffusivity due to the coupling of velocity and temperature fields in natural convection. The enhanced thermal conductivity resulting from the presence of nanoparticles will counteract the impact of the third-grade rheological parameter on the thermal diffusion process. This observation holds considerable importance for solar energy applications, particularly in relation to cooling systems and solar thermal collectors. While the effects of third-grade fluid (non-Newtonian) behavior are significant on velocity development in the annular gap, the influence of temperature is comparatively minimal. This category of non-Newtonian hybrid nanofluids [34,35] provides certain fluid mechanical advantages, offering enhanced stability and no significant loss of thermal efficiency, which is essential for optimizing solar energy harvesting.

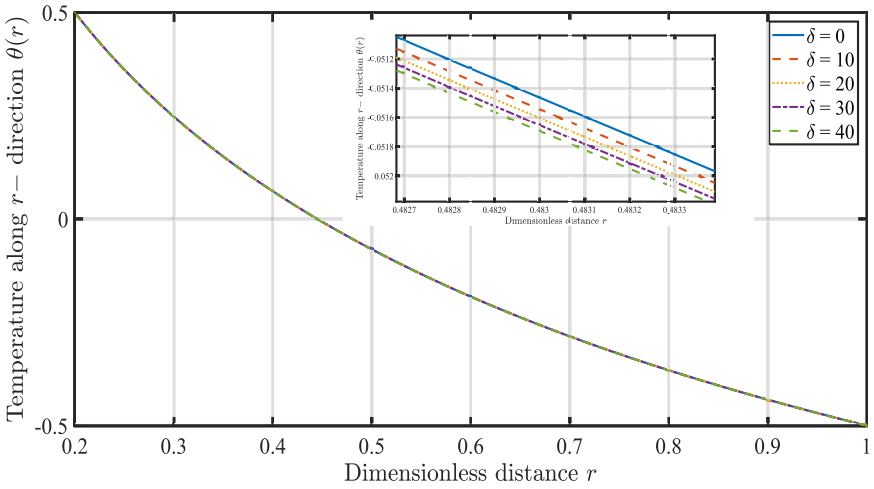

Figure 9: Impact of third-grade fluid parameter (δ) behavior on temperature distributions

Fig. 10 exhibits the consequences of the Grashof number (Γ) on the temperature distribution within the flow. The quadratic thermal buoyancy term, $+\Gamma\left(\frac{(\rho\beta)_{\text{hnf}}}{(\rho\beta)_{\text{bf}}}\tilde{\theta}+\Gamma_1\tilde{\theta}^2\right)$ in Eq. (21) is the only momentum term coupled directly to the energy Eq. (22). A spike in the Grashof number substantially enhances thermal buoyancy, while simultaneously diminishing viscous forces. This process generates intensified free convection currents which boost thermal diffusion and thereby elevate the temperature distribution throughout the annular gap. This phenomenon is very beneficial for solar energy applications, especially in thermal storage systems and solar collectors where incoming heat can be used to mobilize circulation. The higher level of natural convection minimizes thermal resistance, accelerates heat transfer rates, and is advantageous for more efficient thermal management.

This technique serves as essential for sustaining thermal distributions, extending the lifespan of solar thermal components, and optimizing energy collection. Consequently, augmenting the Grashof number i.e., boosting thermal buoyancy is beneficial for optimizing the thermal performance of solar-based energy systems.

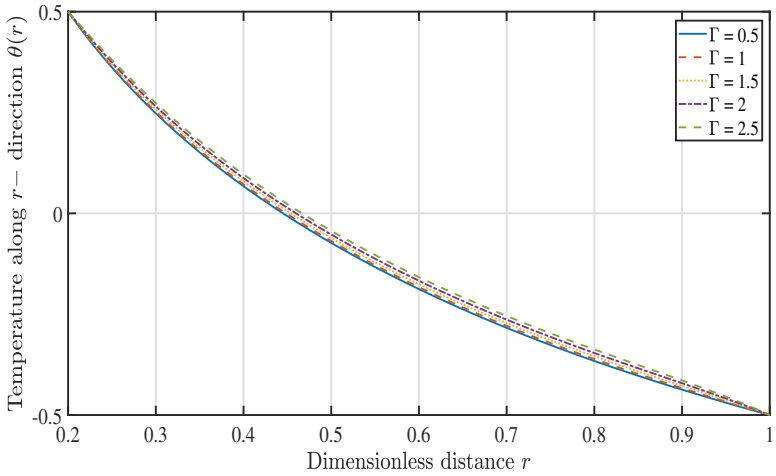

Figure 10: Impact of Grashof number (Γ) behavior on temperature distributions

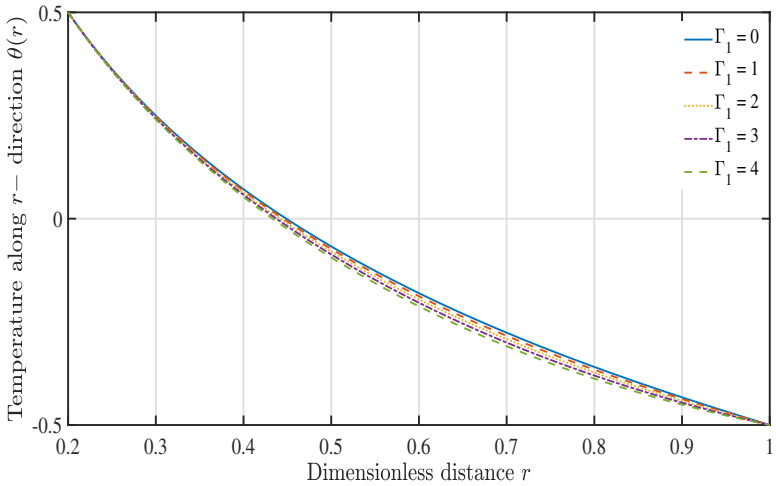

Figure 11: Impact of quadratic convection parameter (Γ_1) behavior on temperature distributions

Fig. 11 demonstrates the effects of the quadratic convection parameter (Γ_1) on the temperature evolution in the annular gap. The quadratic convection parameter inhibits heat diffusion between the concentric cylinders. This process physically implies that nonlinear thermal buoyancy forces aid in stabilizing the fluid when the temperature drastically increases. Consequently, owing to this stabilizing effect, the influence of convective heat transport has lessened, resulting in a reduction of the temperature magnitudes throughout the annular region. In solar energy applications, solar collectors operating at elevated temperatures have limitations in natural convection thermal transport due to larger values of the quadratic convection parameter, consequently reducing the efficiency of thermal

energy distribution. Quadratic convection is effective in preventing thermal disruptions and overheating at high temperatures which may generate thermal corrosion effects at the boundaries of the cylinders. Above a threshold value of the quadratic convection parameter (Γ_1) , higher temperature gradients no longer enhance heat transfer and may, in fact, significantly reduce its effectiveness. Consequently, mathematical models incorporating quadratic convection provide a more robust thermophysical framework for assessing temperature distributions in high-performance solar thermal equipment.

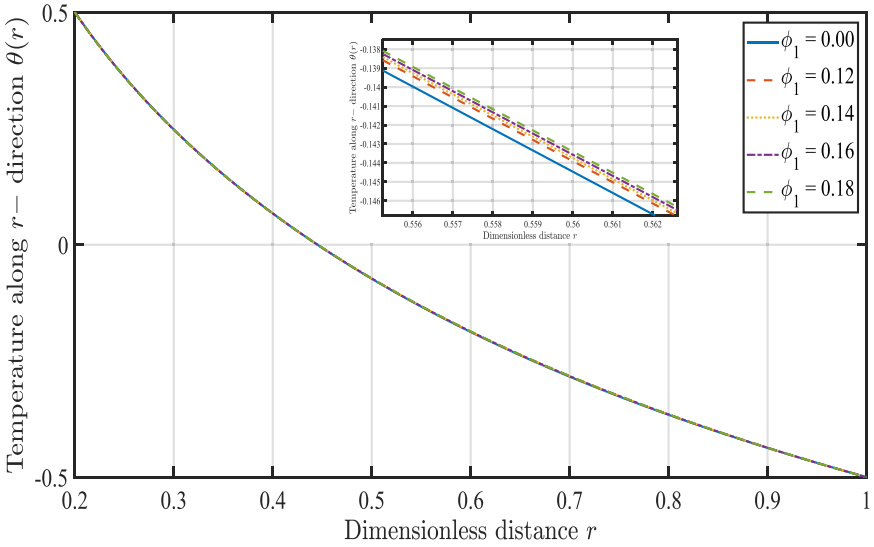

Figure 12: Impact of nanoparticle volume fraction of CNTs (ϕ_1) behavior on the thermal distribution in flow

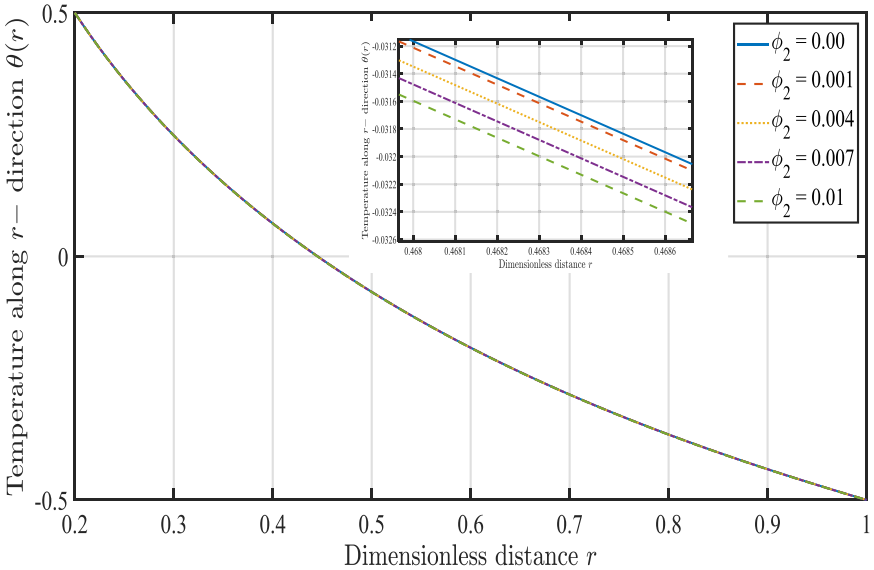

Figure 13: Impact of nanoparticle volume fraction of TiO_2 (ϕ_2) behavior on the thermal distribution in flow

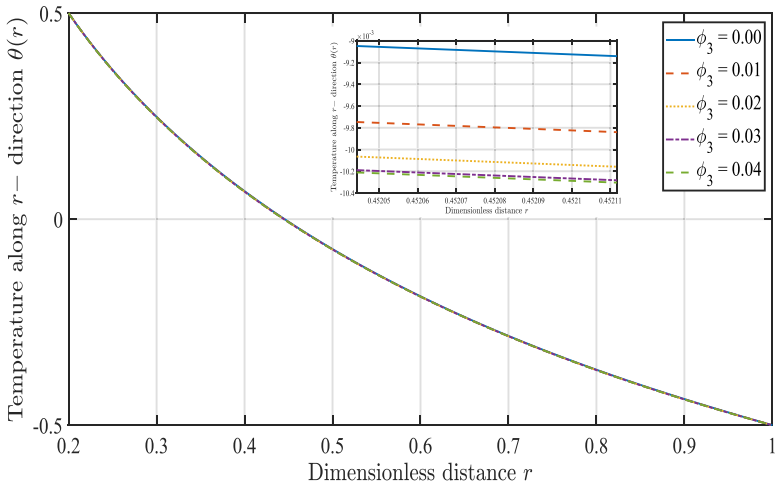

Figure 14: Impact of nanoparticle volume fraction of Al_2O_3 (ϕ_3) behavior on temperature distributions

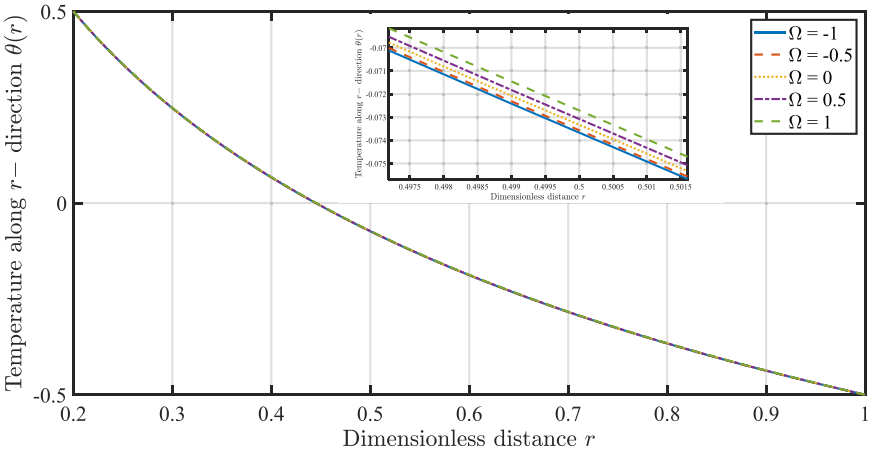

Figure 15: Impact of heat generation and absorption parameter (Ω) behavior on temperature distributions

Fig. 12 exhibits the impact of volume fraction of cylindrical carbon nanotubes (CNTs, ϕ_1) on the temperature distribution inside the flow. This figure illustrates that CNTs improve heat dispersion, although to a minimal extent. This phenomenon arises from the intrinsic morphology and thermal conductivity properties of these unique nanoparticles. Carbon nanotubes provide a superior aspect ratio and exceptional thermal conductivity. Consequently, even at diminished concentrations (lower volume fractions), doping sodium alginate base fluid with CNTs produces a robust thermal conduit which enhances the capacity of the working fluid to retain and transmit heat. This behavior is advantageous in solar energy applications as it improves thermal distribution and heat retention in direct absorber solar collectors (DASCs) resulting in improved thermal performance.

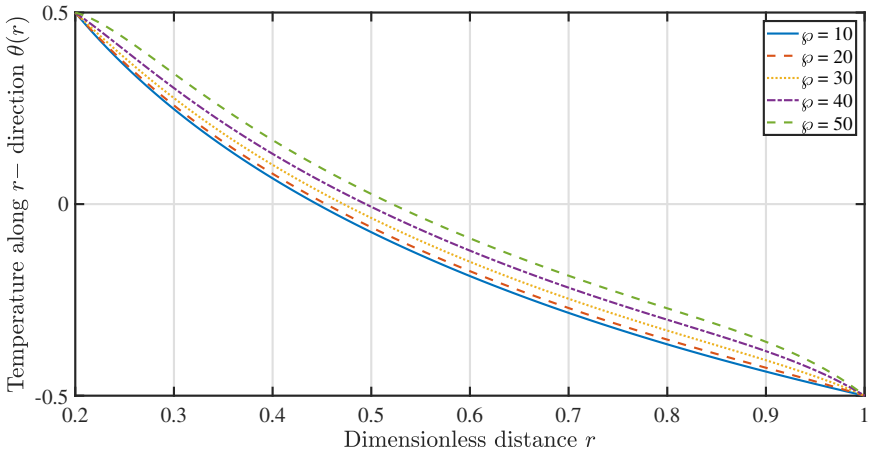

Figure 16: Impact of Prandtl number ($\wp$) behavior on temperature distributions

Fig. 13 displays the influence of volume fraction of spherical Titanium dioxide nanoparticles (TiO_2, ϕ_2) on temperature profiles in the annular zone. This figure implies that TiO_2 nanoparticles have a minor impact on the thermal profiles. A surge in TiO_2 nanoparticle concentration leads to a reduction in the temperature magnitudes. TiO_2 nanoparticles at higher volume fraction suppress thermal diffusion due to their lower aspect ratio, resulting in reduced heat transfer within the hybrid nanofluid. Thus, to achieve optimized performance in nanofluid-based solar thermal systems, it is critical to precisely specify doping percentages (volume fractions) of CNTs.

Fig. 14 displays the impact of volume fraction of platelet-shaped aluminum dioxide nanoparticles (Al_2O_3, ϕ_3) temperature profiles in the annular gap. The thermal profile has been observed to decrease slightly once more due to the increasing influence of doping with Al_2O_3 nanoparticles. Although effective thermal conductors, the alumina nanoparticles still deplete temperatures throughout the entire annular domain due to the extensive surface area of Al_2O_3 nanoparticles. In the context of nanofluid-based solar thermal systems, it is crucial to choose Al_2O_3 nanoparticles in platelet shapes when considering their combination with CNTs. Al_2O_3 nanoparticles, if combined with other nanoparticles, may lead to increased attenuation of temperatures up to critical volume fractions.

Fig. 15 depicts the impact of the heat generation/absorption parameter (Ω) on the thermal distributions in the annular regime. Temperatures clearly exhibit a decreasing pattern for negative values, whereas they display an upward trajectory for positive values of Ω. When $\Omega < 0$, it signifies that the fluid absorbs heat, resulting in a weakening of the thermal distribution. However, when $\Omega > 0$, heat generation occurs, which subsequently accentuates temperature magnitudes. The impact of the heat generation/absorption parameter on the thermal profile is minimal within the range $(-1 \leq \Omega \leq 1)$ when assessed against the primary heat transfer mechanisms, such as thermal buoyancy and nanoparticle shape types.

Fig. 16 indicates the impact of the Prandtl number ($\wp$) on the temperature evolution across the annular gap. Higher Prandtl number improves the temperature magnitudes throughout the entire annulus i.e., with all radial coordinate values. A higher Prandtl number signifies that the viscoelastic nanofluid capacity for heat conduction is modest in contrast to its capacity to impede flow. Consequently, thermal diffusion is modified, and steeper thermal gradients are present. Larger values of the Prandtl number are characteristic of non-Newtonian fluids ($\wp > 10$). Such viscoelastic nanofluids retain a greater amount of heat within the fluid domain, resulting in higher temperature

magnitudes, unlike Newtonian fluids such as water, which have lower Prandtl numbers ($\wp < 10$). In solar energy applications, the significance of the Prandtl number is notable, as a higher Prandtl number indicates enhanced thermal insulation properties of the fluid. This approach proves beneficial when there is a need to maintain heat over extended durations, such as in passive heating patterns and solar thermal energy storage systems. The observed trend indicates that fluids with a higher Prandtl number are capable of maintaining optimized thermal management without significant losses. This enhances the efficiency of energy utilization and contributes positively to maintaining stable operating temperatures in solar collector designs [47,48].

4.3 Skin Friction Profiles

Figs. 17–22 depict the skin friction at the inner wall of the annulus ($r = 0.2$) as opposed to the outer wall of the annulus ($r = 1$), vs. third-grade viscoelastic fluid parameter (δ) for different selected parameters.

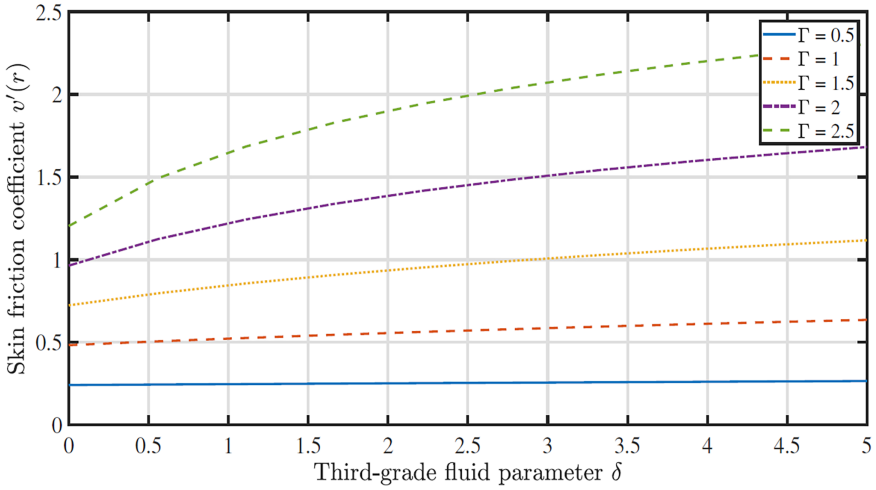

Figure 17: Impact of Grashof number (Γ) on skin friction

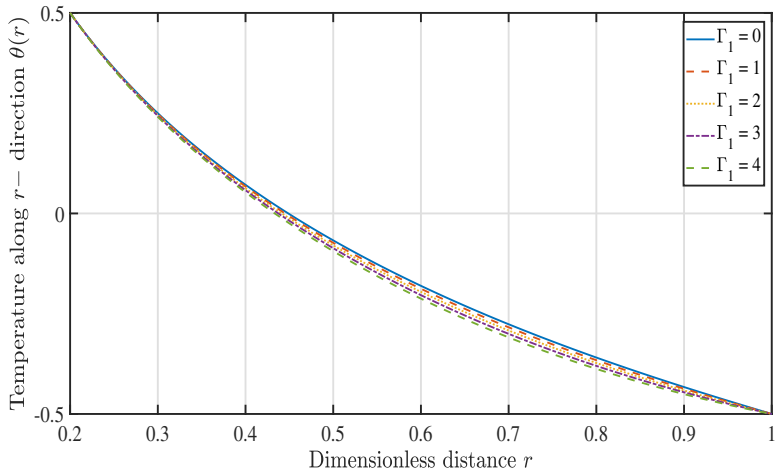

Figure 18: Impact of quadratic convection parameter (Γ_1) on the skin friction

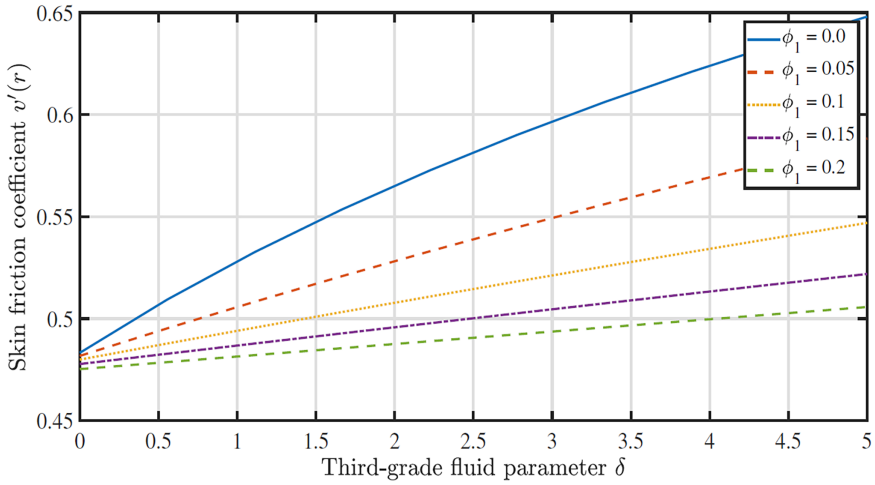

Figure 19: Impact of nanoparticle volume fraction of CNTs (ϕ_1) on the skin friction

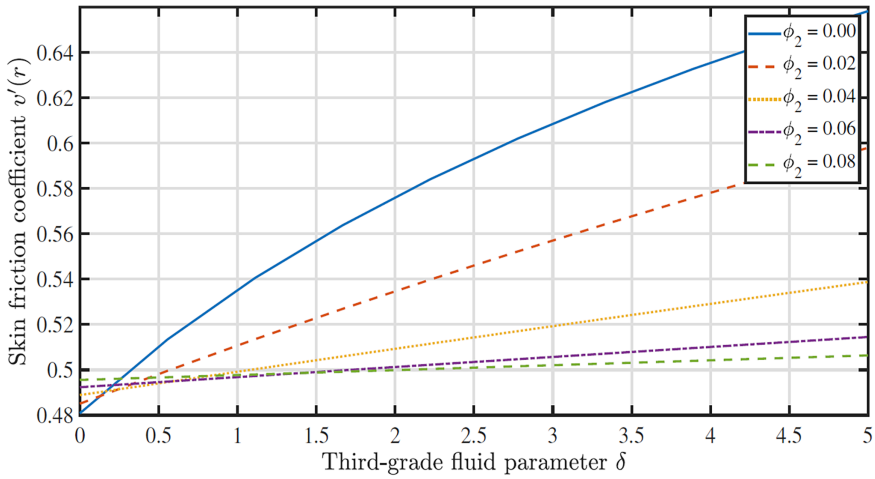

Figure 20: Impact of nanoparticle volume fraction of TiO_2 (ϕ_2) on the skin friction

In all the skin friction plots (except Fig. 18), there is a sustained growth in skin friction with an increment in the third-grade viscoelastic fluid parameter (δ), irrespective of the control parameter being varied. In Fig. 18, the skin friction is found to decay strongly with increment in radial coordinate (abscissa) for all values of non-Boussinesq quadratic convection parameter (Γ_1). For $\delta = 0$, the case of a Newtonian hybrid nanofluid is retrieved, i.e., vanishing viscoelasticity.

Fig. 17 demonstrates that when the Grashof number (Γ) grows, the skin friction profile changes. Increasing the Grashof number indicates buoyancy-driven flow. Elevated skin friction values indicate acceleration of the nanofluid as it shears along the cylinder boundary with intensified velocity gradient. The increment in the Grashof number generates more vigorous convection, resulting in increased resistance at the fluid-solid contact. This will have an impact on solar collector efficiency since heat transmission is influenced strongly by boundary layer interactions. Stronger shearing at the annulus wall in turn modulates the heat transfer rate. Consequently, in industrial engineering, it is

essential for engineers to maintain a balance between the dominant convection forces and the growing surface drag.

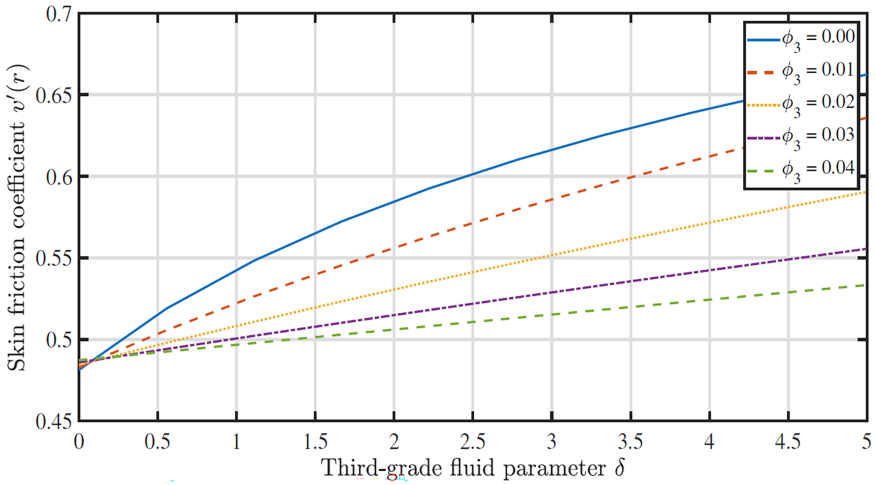

Figure 21: Impact of nanoparticle volume fraction of Al_2O_3 (ϕ_3) on the skin friction

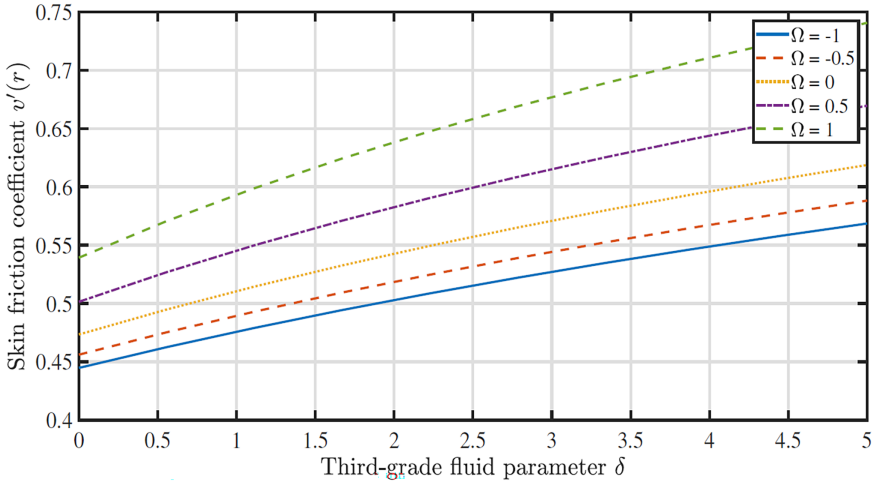

Figure 22: Impact of heat generation/absorption (Ω) behavior on the skin friction

Fig. 18 visualizes the influence of the quadratic convection parameter (Γ_1) on the skin friction profile. The nonlinear thermal buoyancy force generally stabilizes the flow at elevated temperatures. The stabilizing effect dampens convective motion along the boundary wall, resulting in diminished velocity gradients and lower skin friction magnitudes. Quadratic convection effectively acts as a damping force on the annular flow. In solar energy applications, such as solar collectors, passive air heaters, and solar chimneys, the phenomenon of decreased skin friction resulting from quadratic convection is advantageous for minimizing drag effects at the boundaries of the collector and reducing surface wear, hence enhancing material structural integrity. A downside is that stronger quadratic convection produces less mixing in the boundary layer, which diminishes heat transfer efficiency. Consequently, to more accurately predict efficient trade-offs between shear-related energy losses and

thermal transport in solar thermal systems, the inclusion of non-Boussinesq quadratic convection effects is important.

Fig. 19 displays the influence of volume fraction of cylindrical carbon nanotubes (CNTs, ϕ_1) on skin friction. Evidently, higher concentrations of CNTs reduce skin friction values considerably. Despite the remarkable thermal conductivity of CNTs, their prolonged geometric framework affects the flow behaviour by inducing strong deceleration (weakened shearing at the boundary). With a rise in CNT values, the effective viscosity is enhanced due to the elevated surface area, the effects of CNT nanoparticle alignment, and the hydrodynamic resistance is increased. Consequently, the momentum boundary layer thickness is increased near the walls. Furthermore, the cylindrical structure of CNTs tends to counteract the cross-stream momentum, also manifesting in a reduction in the skin friction magnitudes. This is relevant to for example solar thermal transport in annular designs as it effectively increases boundary drag force and may contribute to enhanced heat transfer to the boundary.

Fig. 20 shows the impact of volume fraction of spherical Titanium dioxide nanoparticles (TiO_2, ϕ_2) on skin friction evolution. The figure points out that the skin friction profile reduces with an increase in the volume fraction of TiO_2. However, at the initial stage, when the third-grade fluid parameter, $\delta \approx 0.25$, an opposite trend is discovered. Their spherical shape does not significantly affect flow behavior at low values of material viscoelasticity, as they do not enhance the velocity gradients compared to CNTs, despite TiO_2 having higher thermal conductivity. The growing concentrations of TiO_2 lead to an enhancement in the viscosity of the fluid, while the spherical nature of the TiO_2 nanoparticles generates a mild drag within the fluid, which is attributable to ballistic collisions in the hybrid nanofluid. In compact solar design and solar thermal channels, this kind of process is crucial as it demonstrates reduced resistance, resulting in lowered pumping power required for sustaining natural convection circulation in the annular regime.

Fig. 21 demonstrates the influence of volume fraction of platelet-shaped aluminum dioxide nanoparticles (Al_2O_3, ϕ_3) on the evolution of skin friction profiles. The figure indicates a drop in the skin friction profile as the concentration of Al_2O_3 rises. Platelet-shaped Al_2O_3 nanoparticles possess a flat elliptic structure and a wider surface area, resulting in higher resistance to motion. However, they stabilize the flow behavior while improving the bulk viscosity and suppressing wall shear, which consequently dampens the velocity gradients closer to the wall. This mechanism proves to be beneficial and relevant in low-flow or passive solar configurations, as the reduction in skin friction contributes to an extended operational lifespan and minimized pumping needs.

Fig. 22 demonstrates the response in skin friction distributions with a variation in the heat absorption/generation parameter (Ω) and the skin friction profile. Inspection of the profiles reveals that skin friction magnitudes are amplified with a rise in the heat generation parameter, specifically when $\Omega > 0$. Conversely, it exhibits a declining trend as the heat absorption parameter increases, indicated by $\Omega < 0$. As the heat absorption parameter is boosted, the hybrid nanofluid's capacity to absorb heat also rises, and thermal energy is lost, resulting in diminished thermal gradients and the decreasing impact of the thermal buoyancy-driven flow. When the heat generation parameter is elevated, the thermal distribution within the fluid also grows, which assists the thermal buoyancy forces and mobilizes stronger natural convection currents in the annular flow. The mechanism of heat absorption or generation is clearly a powerful mechanism for modulating internal circulation in solar collector direct absorbers and is equally effective when the working fluid is strongly non-Newtonian (sodium alginate-based fluid). The accentuation in skin friction with stronger heat source effects indicates that a stronger shearing effect is produced at the inner cylindrical boundary, resulting in improved heat transfer.

4.4 Nusselt Number Profiles

Figs. 23–28 plot the variation of the Nusselt number at the inner cylinder wall of the annulus vs. the third-grade fluid parameter (δ) for different values of selected emerging parameters. The Nusselt number indicates the rate of *convective* heat transfer in relation to the conductive heat transfer at the boundary. Generally Nusselt number is found to decay with higher values of the third-grade fluid parameter (δ), i.e., stronger viscoelastity of the hybrid nanofluid.

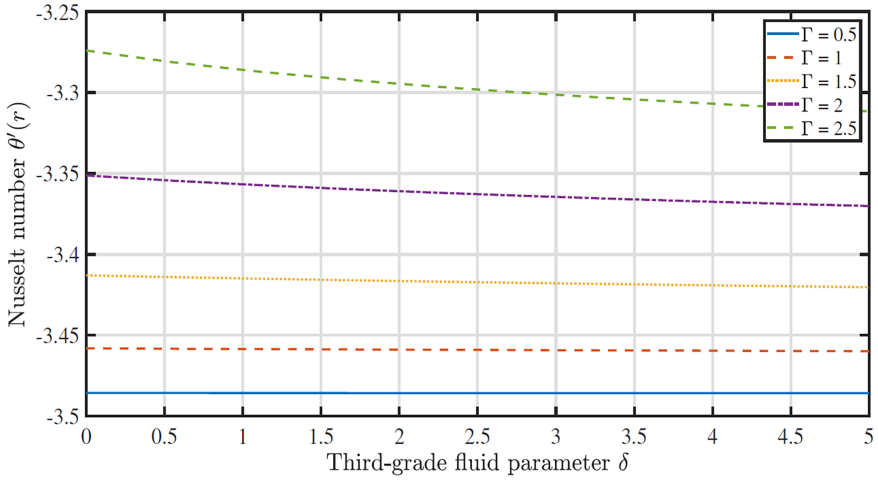

Figure 23: Impact of Grashof number (Γ) on Nusselt number

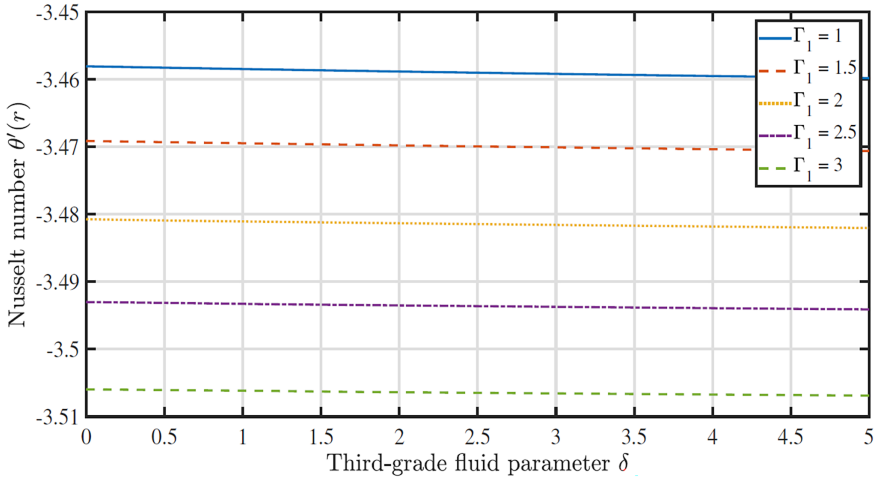

Figure 24: Impact of quadratic convection parameter (Γ_1) on Nusselt number

Fig. 23 depicts the influence of thermal Grashof number (Γ) on the Nusselt number. This figure demonstrates that the Nusselt number increases in proportion to the thermal Grashof number. The buoyancy-driven convection is bolstered by a spike in the Grashof number, which results in amplified heat transfer from the bulk hybrid nanofluid to the boundary owing to the intensified thermal gradients. In a variety of solar energy applications, such as fluid-based solar collectors [47], solar air purifiers, and thermal energy units, the stronger thermal buoyancy associated with larger Grashof number values results in intensification of the natural convection currents and stronger flux of heat

to the boundary, i.e., greater heat transfer. Consequently, it enhances the thermal efficacy and energy extraction of passive solar systems and is more effective than purely forced convection-based systems in which thermal buoyancy effects are absent. This indicates that optimizing the Grashof number can be a valuable strategy to strengthen heat transfer in solar thermal technologies. At low values of Grashof number, the Nusselt number is found to be invariant with third-grade fluid parameter (δ); however, at higher values, there is a strong depletion observed in Nusselt number with increasing δ, i.e., stronger viscoelastity of the hybrid nanofluid.

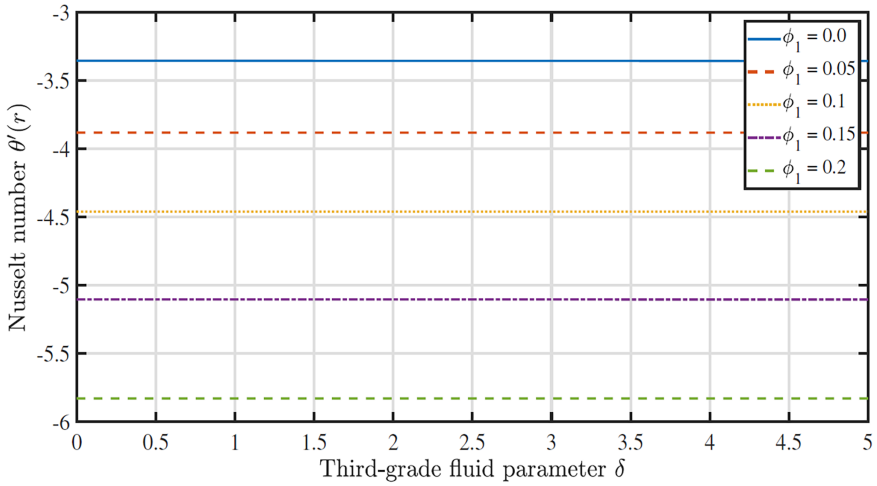

Figure 25: Impact of nanoparticle volume fraction of CNTs (ϕ_1) on Nusselt number

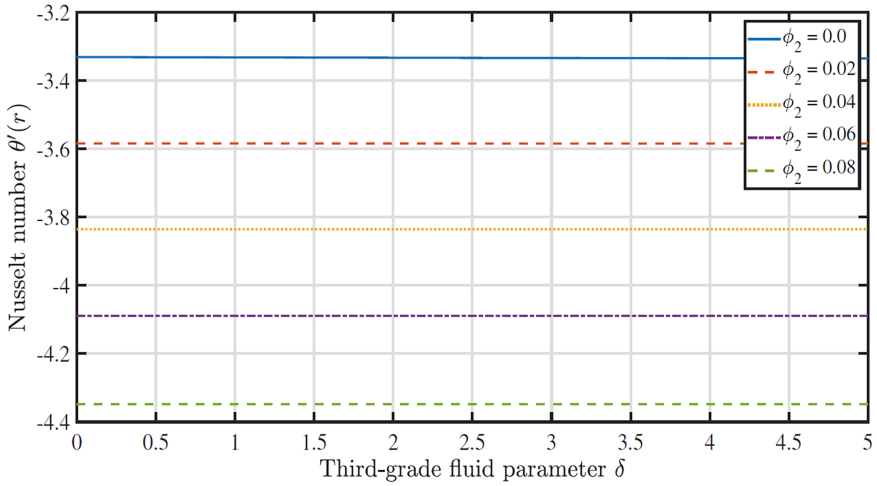

Figure 26: Impact of nanoparticle volume fraction of TiO_2 (ϕ_2) on Nusselt number

Fig. 24 shows the influence of the quadratic convection parameter (Γ_1) on the Nusselt number. Nusselt number exhibits a decreasing pattern as the quadratic convection parameter is boosted. The nonlinear consequences of the buoyancy force at higher thermal gradient are physically captured in the mathematical model by the presence of a quadratic convection parameter. The nonlinear impact of this phenomenon stabilizes the flow and tends to diminish the convective currents in the vicinity of the boundary. This suppresses heat flux to the cylinder wall. The implications of quadratic convection

must be meticulously addressed in solar energy systems that prioritize maximal heat extraction by maximizing operating conditions or making design modifications [48]. A weak reduction in the Nusselt number is computed at all values of the non-Boussinesq quadratic convection parameter (Γ_1) with increasing values of the abcissa cooridnate i.e., third-grade fluid parameter (δ);

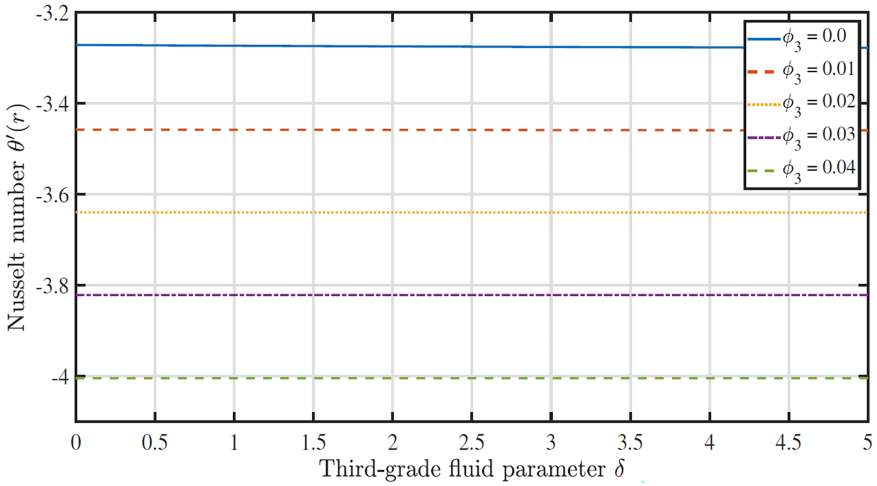

Figure 27: Impact of nanoparticle volume fraction of Al_2O_3 (ϕ_3) on Nusselt number

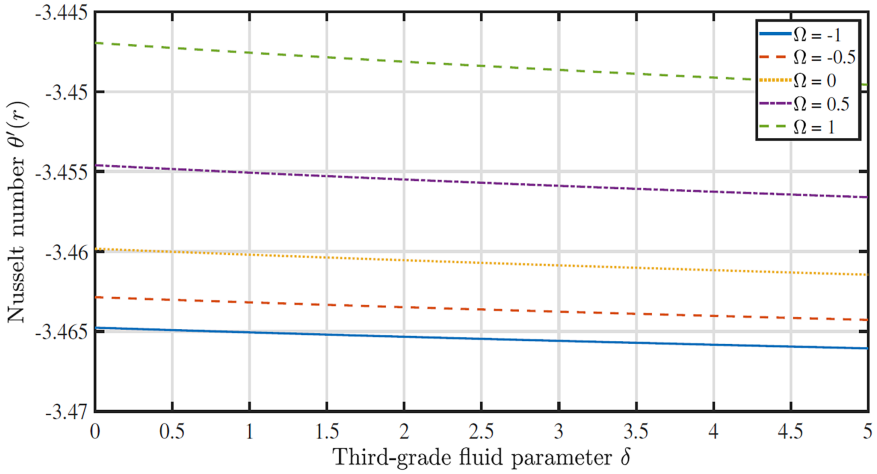

Figure 28: Impact of heat generation and absorption (Ω) behavior on the Nusselt number

Fig. 25 illustrates the effect of volume fraction (concentration) of cylindrical carbon nanotubes (CNTs, ϕ_1) on Nusselt number distributions. It has been observed that the Nusselt number profile diminishes strongly as the volume fraction of CNTs grows to the maximum case of 20% doping ($\phi_1 = 0.2$). It is widely recognized that resistance and effective viscosity are considerably improved by a surge in the volume fraction of CNTs, which is also uniquely connected to their geometrical structures. Consequently, the velocity gradient near the walls is weakened, and the thermal gradient near the wall declines as momentum transport is inhibited. However, this effect is only induced for very strong viscoelasticity in the hybrid nanofluid and is absent for weakly viscoelastic cases (small values of δ). The heat flux to the boundary is therefore stifled, and the Nusselt number is reduced as

a result of the alignment influence and elevated flow resistance that are generated by the cylindrical shape of CNTs. It is judicious for solar collector engineers to strategically deploy CNTs to best exploit their thermophysical advantages, as excessive volume fractions can be counter-productive.

Fig. 26 shows the evolution in Nusselt number profiles with a modification in volume fraction of spherical Titanium dioxide nanoparticles (TiO_2, ϕ_2). Evidently, a strong reduction in the Nusselt number magnitudes is induced with an upsurge in the volume fraction of TiO_2 nanoparticles up to 8% doping ($\phi_2 = 0.08$). The heating effect within the hybrid nanofluid produced with greater nanoparticle doping *draws heat away from the boundary towards the bulk nanofluid*. This, in turn, suppresses *heat flux to the boundary* i.e., *a cooling effect is induced at the wall*. However, the profiles remain only very weakly affected over the entire range of the third-grade material parameter.

Fig. 27 reveals the implications of a modification in the volume fraction of platelet-shaped aluminum dioxide nanoparticles (Al_2O_3, ϕ_3) on the Nusselt number profiles. The Nusselt number (as observed earlier for the CNTs and Titanium dioxide nanoparticles) demonstrates a substantial depletion again as the volume fraction of Al_2O_3 nanoparticles increases to a maximum of 4%. ($\phi_3 = 0.04$). Evidently, with a spike in the volume fraction of Al_2O_3 nanoparticles, a cooling effect is again produced at the inner cylindrical wall of the annular gap since heat is retained in the bulk hybrid nanofluid (confirming the principal objective of nanoparticles as thermal enhancement drivers), and therefore heat flux away from the annular bulk fluid to the boundary is suppressed. This manifests in a depletion in Nusselt number magnitudes as volume fraction is hiked. Thermal management at the boundary is therefore also achievable via nanoparticle doping, and this is consistent across all three types of nanoparticles, although different volume fractions are prescribed for each. As with the other CNT and titanium dioxide nanoparticles, there is very little reduction in Nusselt number induced with increasing third-grade material parameter, at any and all values of the volume fraction of aluminium oxide nanoparticles.

Although in many studies an elevation in Nusselt number with increment in volume fraction of all three hybrid nanoparticles may be generally identified, this is largely confined to *Newtonian base fluids*. It is not necessarily present in gels or viscoelastic base fluids such as sodium alginate, which we considered. While nanoparticles are widely used to enhance heat transfer to boundaries, they can reduce the Nusselt number in specific scenarios, particularly where increased viscosity, larger volume fractions or suboptimal flow regimes dominate. The addition of nanoparticles typically increases the thermal conductivity and viscosity of the base fluid; if the increase in viscosity (pressure drop) outweighs the benefits of improved conductivity, the heat transfer coefficient—and thus the Nusselt number—can decrease. The benefit of this with sodium alginate is that the heat flux to the boundaries is reduced, which enables better thermal management of the collector walls and avoids thermal damage. The heat retention in the bulk fluids can be transported in annular devices more effectively by reducing Nusselt numbers, which implies net heat flux is away from the walls.

Fig. 28 displays the effect of the heat generation/absorption parameter (Ω) on the Nusselt number. As the heat generation variable $\Omega > 0$ rises, it results in the production of internal heat, thereby contributing thermal energy to the third-grade hybrid nanofluid. The process elevates the magnitude of convective heat transfer, promotes buoyancy-driven flow, and elevates thermal gradients, resulting in an enhanced Nusselt number profile. Conversely, a spike in the heat absorption parameter $\Omega < 0$ leads to a reduction in the magnitude of thermal buoyancy, a decline in fluid temperature, and a weakening of convective transport to the boundary. This results in diminished thermal gradients and a *reduction* in the Nusselt number. In solar energy applications, this mechanism can be very beneficial [47], including solar reactors, nanofluid-based storage tanks, and solar thermal collectors. Internal

heat is produced due to exothermic reactions or radiative absorption, although these effects have not been included in the present simulations. An elevated Nusselt number indicates that managing this parameter is beneficial for optimizing heat transfer, which in turn facilitates the achievement of optimal solar heat extraction.

5 Concluding Remarks

This paper examines the natural convection flow of a ternary hybrid nanofluid comprising an incompressible non-Newtonian sodium alginate base fluid with multiple nanoparticles in the annular gap between infinite concentric cylinders, as a model of hybrid annular solar direct absorbers. The study evaluates three types of nanoparticles: Carbon nanotubes, Titanium dioxide, and Aluminum oxide, each with different shapes and different volume fractions. Non-Boussinesq quadratic convection, viscous heating and heat source/sink effects have been included in the mathematical model. The Reiner-Rivlin third-grade differential rheological model and Tiwari-Das formulations for nanoparticle volume fractions have been deployed. The transformed dimensionless nonlinear boundary value problem has then been solved computationally with an efficient finite difference method (FDM) in MATLAB. Validation with previous studies has been included. The influence of key control parameters on velocity distribution, temperature distribution, Nusselt number, and skin friction profiles has been studied. The key points of the present analysis can be summarized as follows:

i. Increasing values of third-grade rheological fluid parameter induce a decrease in radial velocity (strong flow deceleration), whereas elevated Grashof number values improve velocity distribution (flow acceleration) in the annular gap.

ii. Velocity magnitudes exhibit a decreasing trend for higher quadratic (non-Boussinesq) convection parameter values, which stabilize nonlinear buoyancy forces and decelerate the annular flow. With higher volume fractions of CNTs, TiO_2, and Al_2O_3 nanoparticles, there is a significant depletion in velocity magnitudes, induced by the escalation in viscous hydrodynamic forces (greater viscosity). Carbon nanotubes (CNTs) increase the viscosity and density of nanofluids, which generally reduces the flow velocity in solar collector applications. However, this reduction in velocity is often beneficial, as it enhances the heat absorption efficiency of the solar collector. The high viscosity and density of CNT-based nanofluids act as a resistance to flow, which causes the velocity to decrease compared to conventional fluids. Multi-walled carbon nanotubes (MWCNTs) generally flow at a slower rate than single-walled carbon nanotubes (SWCNTs) due to differences in density. While the velocity is generally lower, the overall thermal performance is typically improved due to the enhanced thermal conductivity of the CNTs. Titania nanoparticles are less decelerating in nature and produce higher velocities than CNTs. They influence the kinetic behavior, heat transfer, and flow efficiency of nanofluids in solar collectors by enhancing molecular vibrations, improving thermophysical properties, and facilitating higher working fluid flow rates. While they also increase the viscosity (leading to higher resistance compared to base fluids, but lower resistance compared with CNTs), the net improved heat transfer efficiency often outweighs this drawback, especially in specific solar applications. However, the higher viscosity of titania combined with the base fluid can be managed through proper solar system design to maintain optimal velocity.

iii. Increasing the heat generation (source) parameter improves both the velocity and temperature magnitudes. On the contrary, greater values of heat absorption (sink) exert the opposite influence on both velocity and temperature distributions.

iv. An increment in the third-grade rheological parameter and the quadratic convection parameter reduces temperatures, whereas higher values of the thermal Grashof number and volume fraction of CNTs exhibit the opposite behaviour.

v. Larger values of volume fraction of TiO_2 and Al_2O_3 nanoparticles enhance the temperature distribution.

vi. The skin friction profiles exhibit an increasing trend with an increment in Grashof number, heat generation parameter, and third-grade fluid parameter. In contrast, a boost in the quadratic convection parameter and the greater doping with nanoparticles (CNTs, TiO_2, Al_2O_3) serve to reduce the skin friction magnitudes.

vii. The Nusselt number exhibits a growing pattern as the Grashof number and heat generation parameter rise, whereas this trend is reversed with progressively greater volume fraction of nanoparticles (CNTs, TiO_2, Al_2O_3) and a higher value of non-Boussinesq quadratic convection parameter.

The current study has highlighted some interesting characteristics of annular hybrid non-Newtonian nanofluid transport of relevance to direct absorber solar collectors. However, it has neglected some aspects of multi-physics, including radiative heat transfer, Fourier boundary conditions at the cylinders, and considered only several nanoparticles. Future studies can be developed along several pathways. For example solar radiative heat flux models can be included, alternate rheological models such as the Maxwell upper convected model can be studied for base fluid non-Newtonian characteristics, electroconductive water may be examined with magnetic field modulation, Casson viscoplastic and non-Fourier heat flux models (incorporating thermal relaxation effects) could also be considered. Additionally, one may examine other promising ternary hybrid nanofluids featuring alternate nanoparticles such as Cobalt ferrite ($CoFeO_4$)-Silver (Ag)-Titanium dioxide (TiO_2), gold/silver/hafnium nanoparticles with bioconvection mechanisms may be included, magnetite/cobalt/manganese-zinc nanoparticles and combinations of single and multi-walled CNTs combined with diamond, graphite and graphene nanoparticles may also be simulated to extend the present study. Efforts in these directions are underway and will be reported imminently.

Acknowledgement: Not applicable.

Funding Statement: The authors received no specific funding.

Author Contributions: The authors confirm contribution to the paper as follows: study conception and design: M. M. Bhatti and O. Anwar Bég; methodology: M. M. Bhatti, T. Abbas, and Tasveer A. Bég; formal analysis and interpretation of results: T. Abbas, M. M. Bhatti, and O. Anwar Bég; investigation and implementation: T. Abbas; draft manuscript preparation: T. Abbas and M. M. Bhatti; critical revision of the manuscript: O. Anwar Bég and Tasveer A. Bég; supervision: M. M. Bhatti and O. Anwar Bég. All authors reviewed and approved the final version of the manuscript.

Availability of Data and Materials: All data relevant to this study are contained within the manuscript. As this work is based on numerical modeling and computation, no separate raw dataset is available.

Ethics Approval: Not applicable.

Conflicts of Interest: The authors declare no conflicts of interest.

References

1. Kestin J, Sengers JV, Kamgar-Parsi B, Sengers JMHL. Thermophysical properties of fluid H_2O. J Phys Chem Ref Data. 1984;13(1):175–83. doi:10.1063/1.555707.
2. Assael MJ, Martin Trusler JP, Tsolakis TF. Thermophysical properties of fluids: an introduction to their prediction. Singapore: World Scientific; 1996. doi:10.1142/p007.
3. Paul TC, Morshed AKMM, Fox EB, Khan JA. Enhanced thermophysical properties of NEILs as heat transfer fluids for solar thermal applications. Appl Therm Eng. 2017;110(6):1–9. doi:10.1016/j.applthermaleng.2016.08.004.
4. Fabre E, Sohel Murshed SM. A review of the thermophysical properties and potential of ionic liquids for thermal applications. J Mater Chem A. 2021;9(29):15861–79. doi:10.1039/d1ta03656d.
5. Harrabi I, Hamdi M, Hazami M. Potential of simple and hybrid nanofluid enhancement in performances of a flat plate solar water heater under a typical North-African climate (Tunisia). Environ Sci Pollut Res Int. 2023;30(12):35366–83. doi:10.1007/s11356-022-24703-0.
6. Yıldız G, Ağbulut Ü, Gürel AE. A review of stability, thermophysical properties and impact of using nanofluids on the performance of refrigeration systems. Int J Refrig. 2021;129(1):342–64. doi:10.1016/j.ijrefrig.2021.05.016.
7. Kalsi S, Kumar S, Kumar A, Alam T, Dobrotă D. Thermophysical properties of nanofluids and their potential applications in heat transfer enhancement: a review. Arab J Chem. 2023;16(11):105272. doi:10.1016/j.arabjc.2023.105272.
8. Liu M, Cheng D. Insight into the hydrothermal performance of entropy-optimized time-dependent hybrid nanofluid flow in a non-Newtonian model with solar radiation mechanisms. Therm Sci Eng Prog. 2025;62(1):103647. doi:10.1016/j.tsep.2025.103647.
9. Manjunatha S, Kuttan BA, Jayanthi S, Chamkha A, Gireesha BJ. Heat transfer enhancement in the boundary layer flow of hybrid nanofluids due to variable viscosity and natural convection. Heliyon. 2019;5(4):e01469. doi:10.1016/j.heliyon.2019.e01469.
10. Abdelaziz AH, El-Maghlany WM, Alaa El-Din A, Alnakeeb MA. Mixed convection heat transfer utilizing Nanofluids, ionic Nanofluids, and hybrid nanofluids in a horizontal tube. Alex Eng J. 2022;61(12):9495–508. doi:10.1016/j.aej.2022.03.001.
11. Mandal DK, Biswas N, Manna NK, Gorla RSR, Chamkha AJ. Hybrid nanofluid magnetohydrodynamic mixed convection in a novel W-shaped porous system. Int J Numer Meth Heat Fluid Flow. 2023;33(2):510–44. doi:10.1108/hff-03-2022-0163.
12. Islam MS, Islam S, Siddiki MN. Numerical simulation with sensitivity analysis of MHD natural convection using Cu-TiO_2-H_2O hybrid nanofluids. Int J Thermofluids. 2023;20(23):100509. doi:10.1016/j.ijft.2023.100509.
13. Scott TO, Ewim DRE, Eloka-Eboka AC. Experimental study on the influence of volume concentration on natural convection heat transfer with Al_2O_3-MWCNT/water hybrid nanofluids. Mater Today Proc. 2024;105(7):78–84. doi:10.1016/j.matpr.2023.07.290.
14. Yusuf A, Bhatti MM, Ellahi R. Study of ionic water/graphene nanofluids in solar panels under the effects of thermal radiation and slip conditions using experimental data. Int Commun Heat Mass Transf. 2025;164(6):108845. doi:10.1016/j.icheatmasstransfer.2025.108845.
15. Mebarek-Oudina F, Chabani I, Vaidya H, Ismail AAI. Hybrid-nanofluid magneto-convective flow and porous media contribution to entropy generation. Int J Numer Meth Heat Fluid Flow. 2024;34(2):809–36. doi:10.1108/hff-06-2023-0326.
16. Baithalu R, Mishra SR, Panda S. Magnetic dissipation on radiative free convection of a conducting hybrid nanofluid within a rotating cone and circular disc. Partial Differ Equ Appl Math. 2024;11(22):100788. doi:10.1016/j.padiff.2024.100788.

17. Sai G, Uddin Z, Asthana R. Exploring swirling flow dynamics: unsupervised machine learning in Maxwell hybrid nanofluid convection over an exponentially stretching cylinder with non-linear radiation effects. Commun Nonlinear Sci Numer Simul. 2025;140(9):108378. doi:10.1016/j.cnsns.2024.108378.
18. Xuan Z, Zhai Y, Ma M, Li Y, Wang H. Thermo-economic performance and sensitivity analysis of ternary hybrid nanofluids. J Mol Liq. 2021;323(56):114889. doi:10.1016/j.molliq.2020.114889.
19. Mahboobtosi M, Hosseinzadeh K, Ganji DD. Investigating the convective flow of ternary hybrid nanofluids and single nanofluids around a stretched cylinder: parameter analysis and performance enhancement. Int J Thermofluids. 2024;23(12):100752. doi:10.1016/j.ijft.2024.100752.
20. Kim H, Do Y, Ramachandran S, Sankar M, Thirumalaisamy K. Computational analysis of magnetohydrodynamic ternary-hybrid nanofluid flow and heat transfer inside a porous cavity with shape effects. Phys Fluids. 2024;36(8):082008. doi:10.1063/5.0222802.
21. Shilpa B, Leela V, Badruddin IA, Kamangar S, Ganesan P, Khan AA. Exploration of Arrhenius activation energy and thermal radiation on MHD double-diffusive convection of ternary hybrid nanofluid flow over a vertical annulus with discrete heating. Case Stud Therm Eng. 2025;65(1):105593. doi:10.1016/j.csite.2024.105593.
22. Varatharaj K, Tamizharasi R, Vajravelu K. Ternary hybrid nanofluid flow and heat transfer at a permeable stretching sheet with slip boundary conditions. Eur Phys J Spec Top. 2025;234(8):2293–316. doi:10.1140/epjs/s11734-024-01295-z.
23. Haq F, Ali Ghazwani H, Younis J, Ghazwani MH, Alnujaie A. Numerical investigation of mass and heat transfer in ternary hybrid nanofluid flow with activation energy. Int J Energy Res. 2025;2025(1):8061691. doi:10.1155/er/8061691.
24. Elnaqeeb T, Animasaun IL, Ali Shah N. Ternary-hybrid nanofluids: significance of suction and dual-stretching on three-dimensional flow of water conveying nanoparticles with various shapes and densities. Z Für Naturforschung A. 2021;76(3):231–43. doi:10.1515/zna-2020-0317.
25. Sadeghi-Goughari M, Jeon S, Kwon HJ. Effects of magnetic-fluid flow on structural instability of a carbon nanotube conveying nanoflow under a longitudinal magnetic field. Phys Lett A. 2017;381(35):2898–905. doi:10.1016/j.physleta.2017.06.054.
26. Fan R, Chen X, Wang Z, Custer D, Wan J. Flow-regulated growth of titanium dioxide (TiO_2) nanotubes in microfluidics. Small. 2017;13(30):1701154. doi:10.1002/smll.201701154.
27. Ahmad S, Ali K, Rizwan M, Ashraf M. Heat and mass transfer attributes of copper-aluminum oxide hybrid nanoparticles flow through a porous medium. Case Stud Therm Eng. 2021;25:100932. doi:10.1016/j.csite.2021.100932.
28. Bhatti MM, Anwar Bég O, Ellahi R, Doranehgard MH, Rabiei F. Electro-magnetohydrodynamics hybrid nanofluid flow with gold and magnesium oxide nanoparticles through vertical parallel plates. J Magn Magn Mater. 2022;564(1):170136. doi:10.1016/j.jmmm.2022.170136.
29. Ajeena AM, Farkas I, Víg P. Characterization, rheological behaviour, and dynamic viscosity of ZrO_2-SiC (50-50)/DW hybrid nanofluid under different temperatures and solid volume fractions: an experimental study and proposing a new correlation. Powder Technol. 2024;431:119069. doi:10.1016/j.powtec.2023.119069.
30. Sepehrnia M, Mohammadzadeh K, Hemmati Rozbahani M, Ghiasi MJ, Amani M. Experimental study, prediction modeling, sensitivity analysis, and optimization of rheological behavior and dynamic viscosity of 5W30 engine oil based SiO_2/MWCNT hybrid nanofluid. Ain Shams Eng J. 2024;15(1):102257. doi:10.1016/j.asej.2023.102257.
31. Vicki Wanatasanappan V, Kumar Kanti P, Sharma P, Husna N, Abdullah MZ. Viscosity and rheological behavior of Al_2O_3-Fe_2O_3/water-EG based hybrid nanofluid: a new correlation based on mixture ratio. J Mol Liq. 2023;375:121365. doi:10.1016/j.molliq.2023.121365.

32. Hemmat Esfe M, Toghraie D, Mohammadnejad Ardeshiri E. Experimental study of rheological behavior of MWCNT (50%)-MgO (50%)/SAE40 hybrid nanofluid: dynamic viscosity optimization and numerical simulation of turbulent flow. Ann Nucl Energy. 2023;182(4):109575. doi:10.1016/j.anucene.2022.109575.
33. Aberoumand S, Jafarimoghaddam A, Moravej M, Aberoumand H, Javaherdeh K. Experimental study on the rheological behavior of silver-heat transfer oil nanofluid and suggesting two empirical based correlations for thermal conductivity and viscosity of oil based nanofluids. Appl Therm Eng. 2016;101(1):362–72. doi:10.1016/j.applthermaleng.2016.01.148.
34. Hemmat Esfe M, Alidoust S, Mohammadnejad Ardeshiri E, Kamyab MH, Toghraie D. Experimental study of rheological behavior of MWCNT-Al_2O_3/SAE50 hybrid nanofluid to provide the best nano-lubrication conditions. Nanoscale Res Lett. 2022;17(1):4. doi:10.1186/s11671-021-03639-3.
35. Ravikumar B, Karathanassis IK, Smith T, Gavaises M. Atomistic investigation of viscoelastic nanofluids as heat transfer liquids for immersive-cooling applications. Ind Eng Chem Res. 2024;63(48):21023–37. doi:10.1021/acs.iecr.4c01832.
36. Sharma AK, Tiwari AK, Dixit AR. Rheological behaviour of nanofluids: a review. Renew Sustain Energy Rev. 2016;53(5–8):779–91. doi:10.1016/j.rser.2015.09.033.
37. Fosdick RL, Rajagopal KR. Thermodynamics and stability of fluids of third grade. Proc R Soc Lond A Math Phys Sci. 1980;369(1738):351–77. doi:10.1098/rspa.1980.0005.
38. Hiremath A, Reddy GJ, Bég OA. Transient analysis of third-grade viscoelastic nanofluid flow external to a heated cylinder with buoyancy effects. Arab J Sci Eng. 2019;44(9):7875–93. doi:10.1007/s13369-019-03933-4.
39. Reddy AS, Govindarajulu K, Anwar Bég O, Prasad VR. Entropy generation on hydromagnetic oscillating flow of third grade nanofluid in a porous channel with Cattaneo-Christov heat flux. Indian J Chem Technol. 2023;30:9–22. doi:10.56042/ijct.v30i1.68837.
40. Hiremath A, Reddy GJ, Basha H, Narayanan NSV, Anwar Bég O. Magnetized supercritical third-grade nanofluid flow from a vertical cylinder using a Crank-Nicolson implicit scheme. Waves Random Complex Medium. 2025;35(5):9210–41. doi:10.1080/17455030.2022.2103207.
41. Li S, You X. Shape-factor impact on a mass-based hybrid nanofluid model for homann stagnation-point flow in porous media. Nanomaterials. 2023;13(6):984. doi:10.3390/nano13060984.
42. Ananth Subray PV, Hanumagowda BN, Varma SVK, Hatami M. The impacts of shape factor and heat transfer on two-phase flow of nano and hybrid nanofluid in a saturated porous medium. Sci Rep. 2022;12(1):21864. doi:10.1038/s41598-022-26169-z.
43. Akbar NS, Tripathi D, Bég OA. MHD convective heat transfer of nanofluids through a flexible tube with buoyancy: a study of nano-particle shape effects. Adv Powder Technol. 2017;28(2):453–62. doi:10.1016/j.apt.2016.10.018.
44. Hiremath A, Reddy GJ, Bég OA, Holla H. Numerical investigation on transient third-grade magnetized nanofluid flow and radiative convection heat transfer from a stationary/moving cylinder: nanomaterial and nanoparticle shape effects. Waves Random Complex Medium. 2025;35(1):595–624. doi:10.1080/17455030.2021.2024300.
45. Massoudi M, Christie I. Natural convection flow of a non-Newtonian fluid between two concentric vertical cylinders. Acta Mech. 1990;82(1):11–9. doi:10.1007/BF01173736.
46. Noghrehabadi A, Pourrajab R, Ghalambaz M. Effect of partial slip boundary condition on the flow and heat transfer of nanofluids past stretching sheet prescribed constant wall temperature. Int J Therm Sci. 2012;54(1):253–61. doi:10.1016/j.ijthermalsci.2011.11.017.
47. Simpson T. Solar collectors: theory and applications. New York, NY, USA: Syrawood Publishing; 2023.
48. Kuharat S, Bég OA. Simulation of a nanofluid-based annular solar collector. In: Proceedings of the ICHTFM 2018: 20th International Conference on Heat Transfer and Fluid Mechanics; 2018 Aug 16–17; Istanbul, Turkey.